Available online at www.sciencedirect.com
ScienceDirect
International Journal of Heat and Fluid Flow 28 (2007) 1340–1359
International Journal of HEAT AND FLUID FLOW
www.elsevier.com/locate/ijhff

Experimental study of an impinging jet with different swirl rates

Sergey V. Alekseenko [a,b], Artur V. Bilsky [a], Vladimir M. Dulin [a], Dmitriy M. Markovich [a,b,*]

[a] Institute of Thermophysics, Siberian Branch of RAS, Lavrentyev Avenue 1, Novosibirsk 630090, Russia
[b] Novosibirsk State University, Pirogova street, 2, Novosibirsk 630090, Russia

Received 28 January 2007; received in revised form 22 May 2007; accepted 23 May 2007
Available online 23 July 2007

Abstract

A stereo PIV technique using advanced pre- and post-processing algorithms is implemented for the experimental study of the local structure of turbulent swirling impinging jets. The main emphasis of the present work is the analysis of the influence of swirl rate on the flow structure. During measurements, the Reynolds number was 8900, the nozzle-to-plate distance was equal to three nozzle diameters and the swirl rate was varied from 0 to 1.0. For the studied flows, spatial distributions of the mean velocity and statistical moments (including triple moments) of turbulent pulsations were measured.

The influence of the PIV finite spatial resolution on the measured dissipation rate and velocity moments was analyzed and compared with theoretical predictions. For this purpose, a special series of 2D PIV measurements was carried out with vector spacing up to several Kolmogorov lengthscales.

All terms of the axial mean momentum and the turbulent kinetic energy budget equations were obtained for the cross-section located one nozzle diameter from the impinging plate. For the TKE budget, the dissipation term was directly calculated from the instantaneous velocity fields, thereby allowing the pressure diffusion term to be found as a residual one. It was found that the magnitude of pressure diffusion decreased with the growth of the swirl rate. In general, the studied swirling impinging jets had a greater spread rate and a more rapid decay in absolute velocity when compared to the non-swirling jet.

Keywords: Swirling jet; Impinging jet; Turbulent kinetic energy balance; Stereo PIV; Dissipation

1. Introduction

Impinging jets are widespread in industrial applications, as they have the highest heat and mass transfer rates in the impingement region, and because the transfer coefficients can be effectively controlled by a variety of parameters: nozzle-to-plate distances, Reynolds number of flow, jet array assembly using multiple jet configurations, nozzle shape, external forcing, imposed swirl, etc. The areas of application for impinging jets include paper and fabric drying, local cooling of turbine blades and high-power electronics, material coating, metal solidification, and many others. Some authors also emphasize the importance of impingement study in connection with environment protection from the vertical take-off and landing aircrafts.

Moreover, impinging jets are the objects with a number of physical effects, making them a universal test for CFD modeling. In different flow regions, both free and wall shear layers can be observed, as well as large-scale vortex structures (LSVS) developing in the free jet region and interacting with the impingement surface, a sharp curvature of streamlines in the vicinity of the jet turn, and as a consequence, the appearance of Görtler instability. The PDF of turbulent fluctuations in impinging jet flow is far from the Gaussian distribution due to the presence of LSVS, and anisotropy of pulsations in the near-wall region is quite different from the one at normal boundary layer conditions. Despite the large number of works (starting

* Corresponding author. Address: Institute of Thermophysics, Siberian Branch of RAS, Lavrentyev Avenue 1, Novosibirsk 630090, Russia. Tel.: +7 383 3309040; fax: +7 383 3356684.
E-mail address: dmark@itp.nsc.ru (D.M. Markovich).

0142-727X/$ - see front matter © 2007 Elsevier Inc. All rights reserved.
doi:10.1016/j.ijheatfluidflow.2007.05.011

Notations

Re	Reynolds number
S	swirl rate
TKE	turbulent kinetic energy
Δ	final interrogation area size [m]
x, y, z	Cartesian coordinates in a measurement volume [m]
r, θ, z	radial, azimuthal, and axial directions in a cylindrical coordinate system in a measurement volume
v, w, u	radial, azimuthal, and axial components of fluctuating velocity [m/s]
v', w', u'	intensities of radial, azimuthal, and axial velocity fluctuations [m/s]
u_x, u_y, u_z	components of fluctuating velocity in a Cartesian coordinate system [m/s]
$\mathbf{U} = (V, W, U)$	radial, azimuthal, and axial components of mean velocity [m/s]
U_0	mean flow rate velocity [m/s]
d	nozzle exit diameter [m]
d_1	centerbody diameter [m]
d_2	external diameter of swirler [m]
φ	blade angle [rad]
H	nozzle to impinging plate distance [m]
$\langle\rangle$	ensemble averaging operator
ν	fluid kinematic viscosity [m^2/c]
ε	turbulent kinetic energy dissipation rate [m^2/c^3]
η	Kolmogorov lengthscale [m]
L	integral lengthscale [m]
f	underestimation coefficient

from Gardon and Akfirat, 1965 and Donaldson et al., 1971) devoted to the investigation of heat-mass transfer during turbulent jet impingement, there are only a few experimental studies of impinging jet hydrodynamics which consider the turbulent flow structure in detail. More complete information on the main turbulent characteristics was presented in a paper by Cooper et al. (1993) where the authors performed hot-wire measurements of the average velocity components, RMS pulsations, and the Reynolds stresses for the jet issuing from a round tube and impinging normally onto an obstacle. Landreth and Adrian (1990) presented data on the particle image velocimetry (PIV) measurements of the impinging jet characteristics for the first time. Their results contained distributions of instantaneous velocity and vorticity in the central cross-section of the jet, and also the averaged velocity field near the stagnation point. The mean velocity, Reynolds stresses, and triple correlations were measured with the aid of particle tracking velocimetry (PTV) in the work of Nishino et al. (1996), where the terms of the turbulent kinetic energy balance equation were also obtained.

The development of instabilities in the shear layer of the impinging jet and their effect on the flow structure and transfer coefficients was studied by Didden and Ho (1985), Kataoka et al. (1987), Liu and Sullivan (1996), Alekseenko et al. (1997, 2002) and in the recent work by Vejrazka et al. (2005).

The turbulent structure of jet flow changes significantly under the conditions of a swirl superimposition (see recent works by: Billant et al., 1998; Liang and Maxworthy, 2005). The bases of swirling flows can be found in books by Gupta et al. (1984) and Alekseenko et al. (2003). Depending on the swirl rate and on the manner in which the swirl is applied, substantially different flow regimes can be observed: vortex rings for non-swirling and weakly swirling jets; helical waves with different wavenumbers for strongly swirling jets (Alekseenko et al., 1999). Finally, vortex breakdown appears for high enough swirl rates and is known to have different states: spiral, bubble, or conical, where the last two can be either symmetric or asymmetric (Billant et al., 1998). Superimposition of the external swirl is widely considered as one of the most effective passive ways of flow control. In different kinds of industrial jet devices, the application of swirl induces a reverse flow near the nozzle and leads to a greater spreading rate of the jets, providing larger entrainment of the surrounding media that plays a major role during optimization. In combustion systems, the presence of the recirculation zone caused by a relatively high swirl rate is often used for reliable stabilization of the flame.

There are only a few papers presenting experimental and numerical results on the structure of swirling impinging jets. Some of the authors report a decrease of the transfer coefficients compared to the non-swirling impinging jet flow (Owsenek et al., 1997; Huang and El-Genk, 1998). Azevedo et al. (1997) applied the naphthalene sublimation technique to study the influence of flow parameters on the mass transfer coefficients and determined their overall decrease in the swirling impinging jet for $Re = 9000$–45,000, $H/D = 2$–8 and $S = 0$–0.74. Volchkov et al. (1996) reported that heat transfer coefficients on the surface generally decreased in proportion to the swirl intensity and the impinging distance. However, for an impinging distance less than two nozzle diameters, heat transfer of a swirling impinging jet is enhanced as compared to a conventional circular jet. Recently, Abrantes and Azevedo (2006) performed 2D PIV and LDA measurements in the swirling impinging jets at $Re = 21{,}000$ and confirmed that the presence of a swirl significantly intensified heat transfer from the wall at very small nozzle-to-plate distances, $H/D = 0.25$. In the work of Nozaki et al. (2003), the heat transfer characteristics of the swirling impinging jet at the low Reynolds number of 4,000 were experimentally examined using a combined PIV and planar laser-induced fluo-

rescence (PLIF) technique for simultaneous measurements of velocity and temperature fields. PIV measurements performed at swirl numbers $S = 0.30$ and $S = 0.43$ clearly showed the existence of the recirculation zone in the stagnation region. Authors have shown that the dynamic behavior of recirculation zones mainly affects the turbulent heat transfer at the stagnation region.

On the basis of previous studies, it can be concluded that the application of a swirl is the key for controlling distributions of heat-mass transfer coefficients, especially for jet arrays. On the other hand, an imposed swirl can essentially enhance mixing processes in chemical reactors, burners and mixing devices utilizing confined jet configurations.

The PIV technique allows direct measurement of terms such as the spatial velocity derivatives, the terms of the dissipation rate, spatial spectra, and two-point correlations. However, it is necessary to elaborate a number of complex pre- and post-processing PIV algorithms before calculating the above-mentioned characteristics. "Outliers" linked with the wrong determination of particle displacement are inherent in any PIV processing method. Therefore, the stages of raw velocity field validation, false vector removal (Westerweel, 1994) and "empty holes" interpolation (Foucaut et al., 2000) are needed before further post-processing steps. For accurate calculation of instantaneous velocity gradients, a proper derivative filter should be implemented (Foucaut and Stanislas, 2002). Heinz et al. (2004) demonstrated that the presence of outliers essentially affected the accuracy of the high order statistical moments calculation and proposed a statistical validation algorithm based on the PDF of velocity fluctuations modeling. Piirto et al. (2003) have shown that the statistical characteristics of turbulence measured by PIV are underestimated for a low spatial resolution, especially for the dissipation rate. In the present paper the correction of dissipation was proposed using Pao's model for the TKE spectrum function.

The objective of the present work is to study, with the aid of PIV and Stereo PIV, the hydrodynamic structure of impinging jet flow with superimposed swirl. The main emphasis was on obtaining spatial distributions of statistical characteristics and a calculation of the turbulent kinetic energy budget.

2. Experimental setup, apparatus and data processing

The experimental setup represented a hydrodynamic loop equipped with a pump, a flowmeter, and a temperature stabilizing device. The jet flow was organized in a transparent rectangular working section (40 cm height, 20 cm width, 20 cm length). A circular nozzle with a Vitoshinsky profile (contraction 1:16 in area) and an exit diameter of $d = 15$ mm was mounted at the bottom of the working section (see Fig. 1). An axisymmetric jet flow issued upwards from the nozzle and impinged on a flat plate. The distance between the nozzle exit and the impingement plate was $H = 45$ mm, corresponding to the ratio $H/d = 3$. Water flow was driven by a pump which had a rotation speed precisely controlled by an inverter. The Reynolds number, defined on the basis of mean flow rate velocity $U_0 = 0.52$ m/s and nozzle diameter, was equal to 8900. A thermostat was used to maintain a constant water temperature of 26 °C with an accuracy of ± 0.2 °C. The choice of these flow conditions was due to peculiarities of the impinging jet flow configuration. The present Reynolds number and the nozzle-to-plate distance provide a transitional flow regime where large scale vortex structures developing in the jet shear layer are clearly pronounced and reach the impinging plate before their break-up in a non-swirled jet (see Alekseenko et al., 2002).

The present work studies non-swirling (referred to below as "conventional") and swirling impinging jets where the measurement plane (r, z) contains the jet axis. The schemes of the studied flows and the measurement zones locations are shown in Fig. 2. The "PIV-IT" Stereo PIV system developed at the Institute of Thermophysics was used for the measurements. The system consisted of a double cavity Nd:YAG pulsed laser (50 mJ), couple of CCD (1240×1024 pix^2) cameras and a synchronizing processor. A laser sheet was formed by a cylindrical lens and had a minimal thickness of 0.5 mm in the measurement section, controlled using a focusing lens. Depending on the measurement area size, polyamide particles or silver-coated hollow glass spheres with different mean diameters (20, 10 or 5 μm) were used for flow seeding. During the experiments, the system was operated by a computer with "ActualFlow" software. The software exploits algorithms presented at the previous

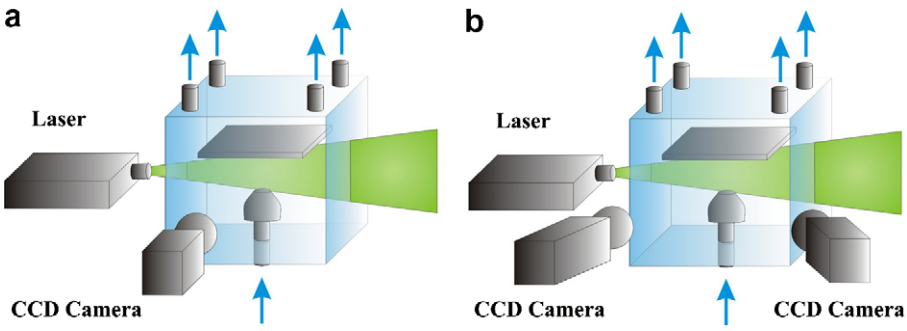

Fig. 1. Sketch of experimental setup. (a) Non-swirling impinging jet and (b) swirling impinging jet.

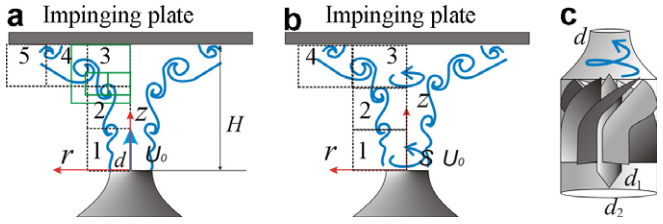

Fig. 2. Schemes and measurement areas locations for non-swirling (a) and swirling (b) impinging jet and (c) sketch of swirler arrangement.

two "PIV Challenge" Symposia in 2003 and 2005 by the "IOT" team. Detailed information about the proceeding algorithms can be found in Stanislas et al. (2005, in press).

In the first stage of the measurements, the conventional impinging jet was studied using 2D2C PIV. A top-hat exit velocity profile with a momentum thickness of 0.25 mm was organized by the nozzle. Two smoothing grids were mounted in the plenum chamber of the nozzle. In order to provide a high enough spatial resolution (up to 0.26 mm/vector), the whole measurement area was separated into five elementary zones (see Fig. 2a) where the measurements were performed independently. For each zone, 1500 image pairs were captured and processed by an iterative cross-correlation algorithm with image deformation. During processing, the final interrogation area (IA) size was 32×32 pixels with 50% overlap. In addition, a set of PIV measurements was carried out in which the flow was studied with various spatial resolutions. This was done in order to study the influence of the ratio of the IA size and the Kolmogorov lengthscale on measured turbulence characteristics. In this case, independent measurements were performed in the elementary zones shown in Fig. 2a at the distance $z = 2d$ from the nozzle exit, and 3000 image pairs were captured for each zone. A summary of the experimental conditions is presented in Table 1.

At the second stage, swirling impinging jets were studied with the aid of the Stereo PIV technique. For the organization of the swirling jet flow, swirl generators with different blade angles were put into the plenum chamber before the convergent nozzle exit (see Fig. 2c). The definition of a swirl rate (1), following Gupta et al. (1984), was based on geometric parameters:

$$S = \frac{2}{3}\left(\frac{1-(d_1/d_2)^3}{1-(d_1/d_2)^2}\right)\tan(\varphi) \qquad (1)$$

Table 1
Conditions of image acquisition during the measurements, spatial resolutions and correction coefficients for the studied flows

Swirl rate	Measurement area size [mm^2]	# of areas	# image pairs	Δ [mm]	Δ/η	$1/f_\varepsilon$
$S = 0$	15.9×15.9	5	1500	0.52	13.9	2.86
$S = 0$	29.7×22.47	1	3000	0.76	20.2	5.2
$S = 0$	9.9×7.87	2	3000	0.25	6.8	1.0
$S = 0.41$	24.5×19.0	4	3000	0.68	13.7	2.9
$S = 0.70$	24.5×19.0	4	3000	0.68	14	–
$S = 1.0$	24.5×19.0	4	3000	0.68	15.4	3.6

Here, $d_1 = 7$ mm is the diameter of the centerbody supporting the blades, $d_2 = 27$ mm is the external diameter of the swirler, and φ is the blade inclination angle. During the experiments, the swirl number was varied from 0.41 to 1.0 by using the swirlers with different blade angles. The whole measurement area was separated into four elementary zones (see Fig. 2b), for which 3000 image pairs were captured by each of two cameras. For image processing, the above-mentioned iterative cross-correlation algorithm was used. The angle between the optical axis of each camera (see Fig. 2b) and the measurement plane normal was 26°. A plane calibration target with the size of 25×25 mm^2 was employed for a stereo calibration. During the calibration, a third-order polynomial transform was used to minimize non-linear optical distortions.

For all studied cases, a number of post-processing procedures were implemented. Instantaneous velocity fields were validated and "outliers" were removed using the adaptive median filter (Westerweel and Scarano, 2005) and signal-to-noise ratio (SNR) criteria for cross-correlation maxima. Before the stereo reconstruction or spatial derivatives calculation, a third-order 3×3 linear interpolation filter was used for the "holes" interpolation. In the present work for the derivatives estimation, the second-order centered difference scheme was used, which is considered as the optimal one in the case of a 50% IA overlap (according to Raffel et al., 1998; Foucaut and Stanislas, 2002). A statistical filtering procedure (Heinz et al., 2004) based on the model PDF of fluctuating velocity was implemented in order to achieve an accurate high-order moments calculation. In general, sources of PIV measurement uncertainty can be separated into several main groups. The first one arises from the unavoidable imperfections of the experimental setup: optical distortions, misalignment of the laser sheet and calibration target planes during stereo measurements, quality of flow seeding, out-of-plane motion effects, etc. The second source of error is a general processing error associated with the camera noise, effects of sampling (e.g. peak-locking effect), high frequency data noise from the FFT of non-periodic IA, and others. The numerous tests of adaptive processing algorithms based on synthetic images show this error to be below 0.1 pix, which corresponds to about 2% for a particle displacement of 5 pix. The third source of error is connected with the averaging over IA when the cross-correlation function is being calculated. When studying turbulent flows at a high Re number, limited spatial resolution of PIV leads to an underestimation of turbulent characteristics. As shown in Section 3.3 of the present paper, this error can be up to 30% and 50% for the second- and third-order moments, respectively, and up to 100% for the dissipation rate. In this paper, the first and second types of errors will be estimated by the magnitude of the RMS velocity fluctuations in the regions where the flow is almost absent. Additional attention will be drawn to the spatial resolution of the PIV in Section 3.3.

3. Results and discussion

3.1. Governing equations

The studied impinging jets have a general axial symmetry, and thus can be described using a cylindrical coordinate system where all derivatives in the azimuthal direction can be assumed to be zero. The coordinates (r,θ,z) denote the radial, azimuthal, and axial directions, respectively. Correspondingly, (V,W,U) and (υ,w,u) are the radial, azimuthal, and axial components of the mean and fluctuating velocity. Using the axisymmetric conditions for the incompressible stationary flow, the axial mean momentum (AMM) transport equation is given by (2):

$$-\left(U\frac{\partial U}{\partial z}+V\frac{\partial U}{\partial r}+\frac{W}{r}\cancel{\frac{\partial U}{\partial\theta}}\right)-\left(\frac{\partial\langle u^2\rangle}{\partial z}+\frac{1}{r}\frac{\partial\left(r\langle u\upsilon\rangle\right)}{\partial r}+\frac{1}{r}\cancel{\frac{\partial\langle uw\rangle}{\partial\theta}}\right)-\frac{1}{\rho}\frac{\partial P}{\partial z}+\nu\left(\frac{\partial^2U}{\partial z^2}+\frac{1}{r}\frac{\partial}{\partial r}\left(r\frac{\partial U}{\partial r}\right)+\frac{1}{r^2}\cancel{\frac{\partial^2U}{\partial\theta^2}}\right)=0 \tag{2}$$

Here, ρ denotes flow density, P is the mean pressure, ν is the kinematic viscosity and $\langle\rangle$ indicates ensemble averaging. The eliminated terms in (2) appear to be zero due to the rotational symmetry of the flow. The first and second bracketed terms in the left-hand side of Eq. (2) correspond to convection and turbulent diffusion, while the third and fourth bracketed terms correspond to transport by the mean pressure gradient and viscous diffusion, respectively. The turbulent kinetic energy (TKE) budget equation is given by (3):

$$-\left(U\frac{\partial\langle q^2\rangle}{\partial z}+V\frac{\partial\langle q^2\rangle}{\partial r}+\frac{W}{r}\cancel{\frac{\partial\langle q^2\rangle}{\partial\theta}}\right)-\left(\frac{\partial\langle uq^2\rangle}{\partial z}+\frac{\partial\left(r\langle\upsilon q^2\rangle\right)}{r\partial r}+\frac{1}{r}\cancel{\frac{\partial\langle wq^2\rangle}{\partial\theta}}\right)-\frac{1}{\rho}\left(\frac{\partial\langle up\rangle}{\partial z}+\frac{\partial\left(r\langle\upsilon p\rangle\right)}{r\partial r}+\frac{1}{r}\cancel{\frac{\partial\langle wp\rangle}{\partial\theta}}\right)+\nu\left(\frac{\partial^2\langle q^2\rangle}{\partial z^2}+\frac{1}{r}\frac{\partial}{\partial r}\left(r\frac{\partial\langle q^2\rangle}{\partial r}\right)+\frac{1}{r^2}\cancel{\frac{\partial^2\langle q^2\rangle}{\partial\theta^2}}\right)-\left(\begin{array}{l}\langle u^2\rangle\frac{\partial U}{\partial z}+\langle\upsilon^2\rangle\frac{\partial V}{\partial r}+\langle w^2\rangle\left(\frac{1}{r}\cancel{\frac{\partial W}{\partial\theta}}+\frac{V}{r}\right)+\langle u\upsilon\rangle\left(\frac{\partial V}{\partial z}+\frac{\partial U}{\partial r}\right)\\ +\langle\upsilon w\rangle\left(\frac{1}{r}\cancel{\frac{\partial V}{\partial\theta}}+\underline{\frac{\partial W}{\partial r}}-\underline{\frac{W}{r}}\right)+\langle uw\rangle\left(\frac{1}{r}\cancel{\frac{\partial U}{\partial\theta}}+\underline{\frac{\partial W}{\partial z}}\right)\end{array}\right)-\varepsilon=0 \tag{3}$$

where $q^2=(\upsilon^2+w^2+u^2)/2$ is the turbulent kinetic energy. Similar to the AMM transport Eq. (2), the crossed terms vanish for the axisymmetric flow. The underlined terms in (3) appear for swirling jets only, i.e., when $W\neq 0$. The first and second bracketed terms on the left-hand side of (3) correspond to convection and turbulent diffusion. The third and fourth bracketed terms represent pressure and viscous diffusion. The fifth and sixth bracketed terms indicate shear production and the TKE dissipation rate (ε). The dissipation rate is the most challenging part to estimate in the balance equation because all spatial derivatives should be calculated and a high spatial resolution should be provided during the measurements. When the dissipation rate is presented in the cylindrical coordinate system, terms containing a negative power of r (e.g. $2\nu\langle\left(\frac{\partial w}{\partial r}-\frac{w}{r}\right)\left(\frac{\partial u}{r\partial\theta}\right)\rangle$) will appear in the equation, leading to a high uncertainty near $r=0$ during calculations using raw experimental data. To avoid this problem, the complete equation for the dissipation rate is used in Cartesian coordinates:

$$\varepsilon=\nu\left\langle 2\left(\frac{\partial u_x}{\partial x}\right)^2+2\left(\frac{\partial u_z}{\partial z}\right)^2+2\left(\underline{\frac{\partial u_y}{\partial y}}\right)^2+\left(\frac{\partial u_x}{\partial z}+\frac{\partial u_z}{\partial x}\right)^2+\left(\underline{\frac{\partial u_x}{\partial y}}+\frac{\partial u_y}{\partial x}\right)^2+\left(\underline{\frac{\partial u_z}{\partial y}}+\frac{\partial u_y}{\partial z}\right)^2\right\rangle \tag{4}$$

Here, coordinates (x,y,z) and the components of the fluctuating velocity (u_x,u_y,u_z) are codirectional with (r,θ,z) and (υ,w,u), corresponding to the plane coincident with the jet axis. The underlined terms in (4), corresponding to the derivatives in the normal-to-plane direction, cannot be measured directly using the one-plane Stereo PIV approach. Alekseenko et al. (submitted for publication) have shown that Eq. (5) is quite appropriate for estimating the dissipation in the free round jet.

$$\varepsilon\approx\nu\left\langle 4\left(\frac{\partial u_x}{\partial x}\right)^2+2\left(\frac{\partial u_z}{\partial z}\right)^2+3\left(\frac{\partial u_x}{\partial z}+\frac{\partial u_z}{\partial x}\right)^2\right\rangle \tag{5}$$

In approximation (5), several conditions were used which result from the axial symmetry over the z axis. (5) does not use the assumption of local flow homogeneity, which appears in the local axisymmetry condition introduced by George and Hussein (1991) and in the local isotropy condition.

3.2. Mean velocity, second- and third-order moments

This section of the work presents the measured turbulence statistics for the impinging jets. On the basis of the estimated 3C velocity fields, the spatial distributions of the statistical moments of fluctuating velocity were calculated for the studied flows. Inflow conditions strongly depend on the type of swirl generator used (rotating pipe with or without contraction nozzle, swirlers). Distributions of the axial and azimuthal mean velocity are presented in Fig. 3 for the cross-section close to the nozzle exit ($z/d\approx 0.01$). The magnitude of the radial mean velocity was found to be rather small (about 15 times less than U_0) and is not plotted. It can be seen that the values of U for the swirling jets reach almost zero at $r=0$. The intensities of the axial, radial, and azimuthal velocity fluctuations near the nozzle exit are presented in Fig. 4. For a conventional jet, the turbulence intensities in the radial and axial directions are 9.2% and 2.3% of U_0 at the jet axis, respectively. The swirling jet flows have significantly larger magnitudes and reach 50% because of the swirler arranged inside the nozzle. In order to obtain an upper estimate of the error connected with the accuracy of processing algorithms and the optical system arrangement, the RMS of the velocity components were calculated for the range of $r>1.5d$ at $z/d\approx 0.01$, where the flow was assumed to be

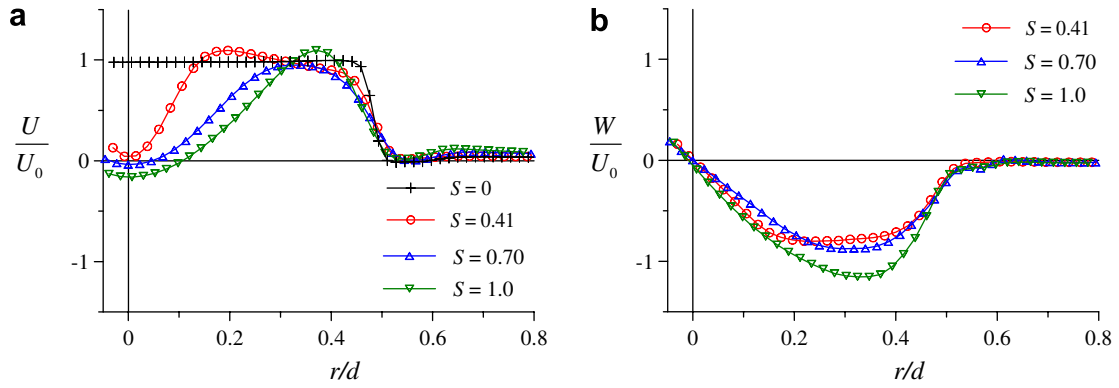

Fig. 3. Distributions of the axial (a) and azimuthal (b) mean velocity near the nozzle exit ($z/d \approx 0.01$) for the impinging jet flows.

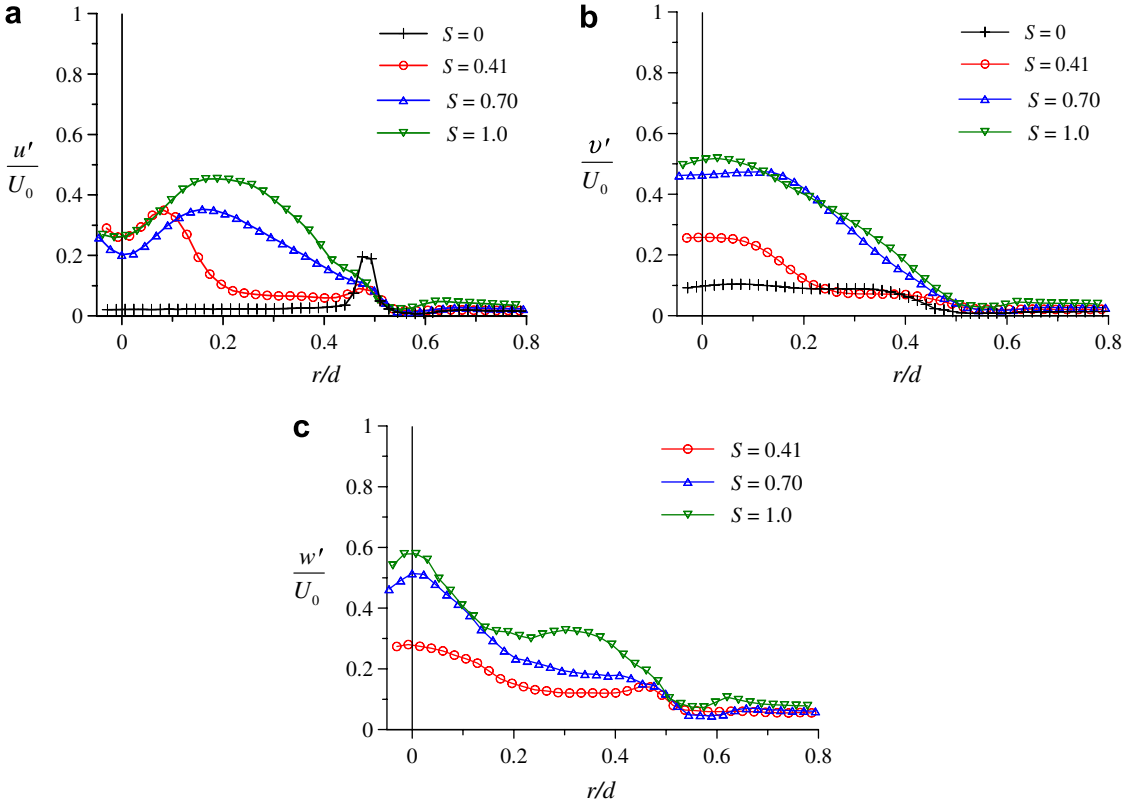

Fig. 4. Distributions of intensities of the axial (a), radial (b) and azimuthal velocity fluctuations near the nozzle exit ($z/d \approx 0.01$) for the impinging jet flows.

negligible. For the $S = 0$ case, the RMS velocity was around 3% of U_0. The RMS values of the in-plane velocity for the $S = 0.41$, $S = 0.70$, and $S = 1.0$ cases were 3.5%, 4.5%, and 4.7% of U_0, respectively. The RMS values of the out-of-plane velocity were found to be 5.2%, 5.8%, and 7.3% for the $S = 0.41$, $S = 0.70$, and $S = 1.0$ cases. These results are in general agreement with theoretical analysis by Lawson and Wu (1997), which showed that in the stereo PIV experiment, the error in out-of-plane velocity estimation is expected to be higher than that for in-plane velocity. As was shown by Heinz et al. (2004), the main source of error in measurements of the high-order moments by PIV is the presence of unfiltered outliers. In the present work, this issue was removed by the application of proper validation procedures. Total error also includes the effect of the spatial averaging, which is discussed in Section 3.3.

In Fig. 5, the examples of instantaneous velocity and vorticity fields for the impinging jet at $S = 0$ and $S = 0.70$ are shown. For the conventional jet, ring-like large-scale vortex structures develop in the jet's mixing layer according to the Kelvin–Helmholtz instability scenario, and represent the result of several events of smaller vortex pairing. For the jet at $S = 0.70$, intense vortex

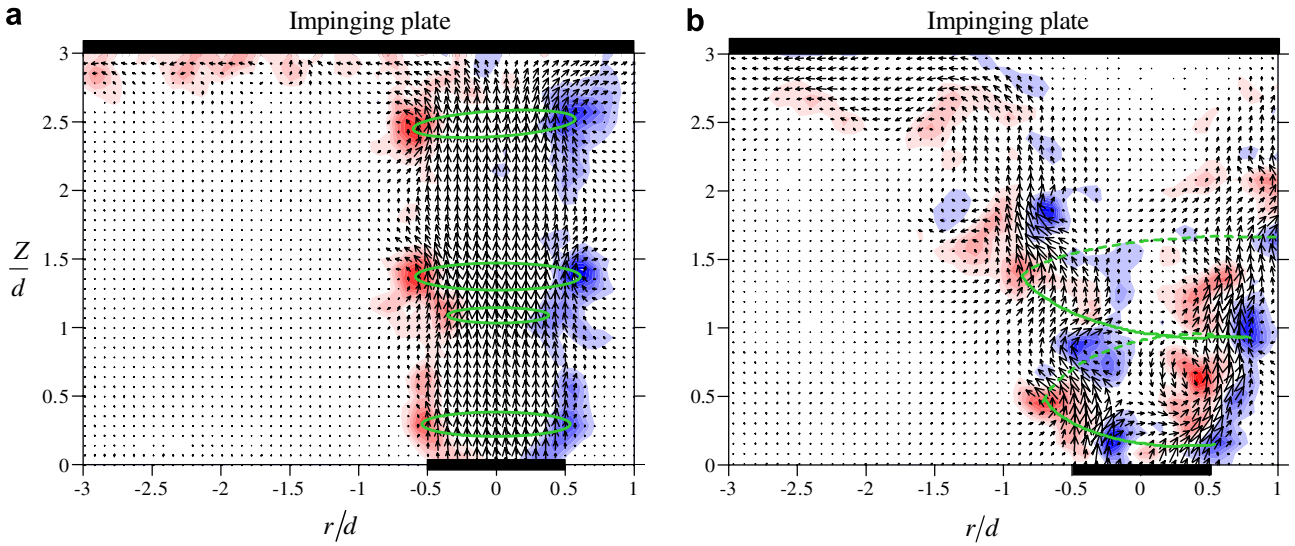

Fig. 5. Instantaneous velocity and vorticity fields. Impinging jet at (a) $S = 0$ and (b) $S = 0.70$.

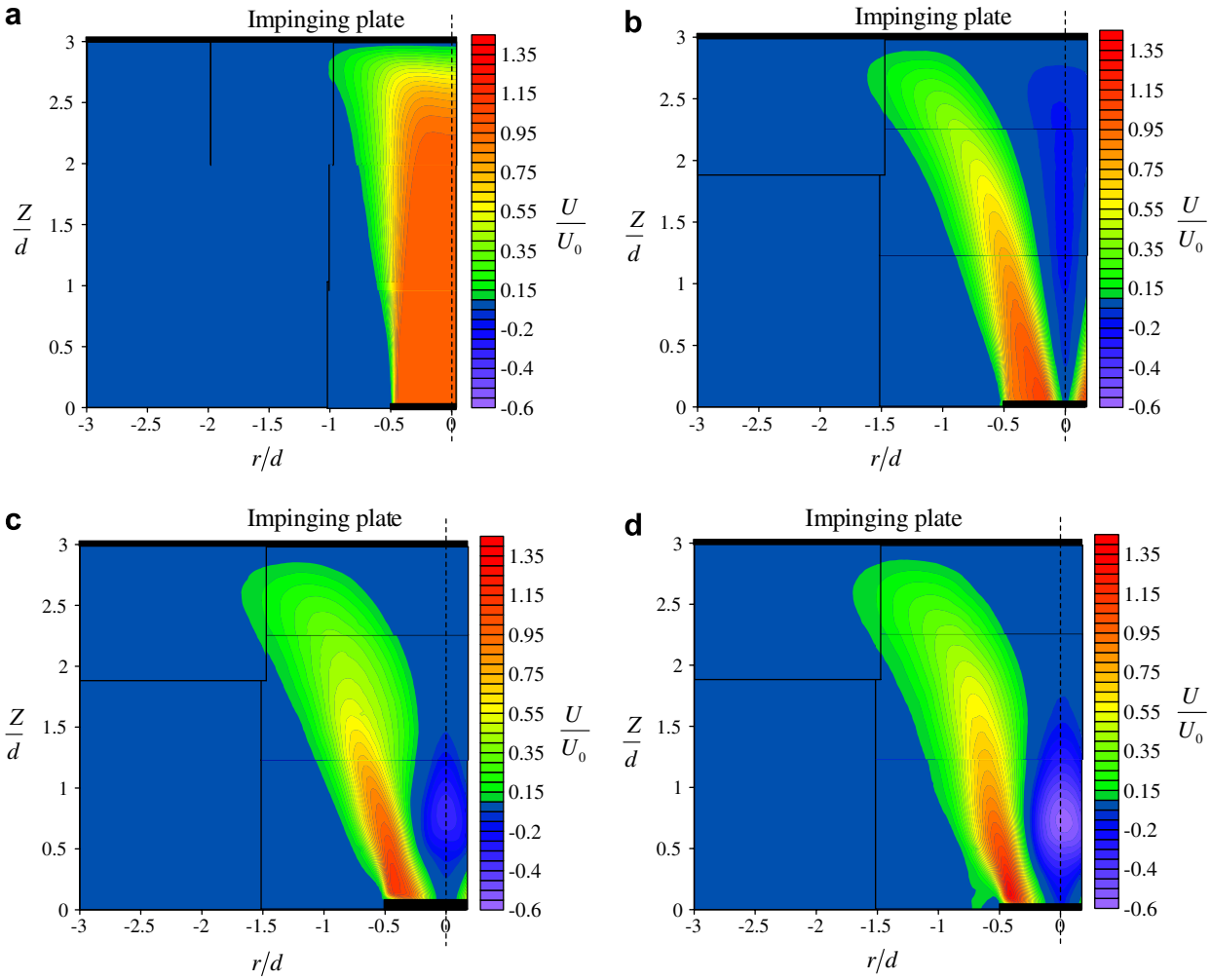

Fig. 6. Distributions of the normalized axial component of mean velocity in the impinging jets. (a) $S = 0$, (b) $S = 0.41$, (c) $S = 0.70$ and (d) $S = 1.0$.

spirals are observed and the breakdown of the flow symmetry directly from the origin takes place. During the study of the swirling impinging jet at $S = 0.70$ and $S = 1.0$, the recirculation zone was clearly observed near the nozzle exit.

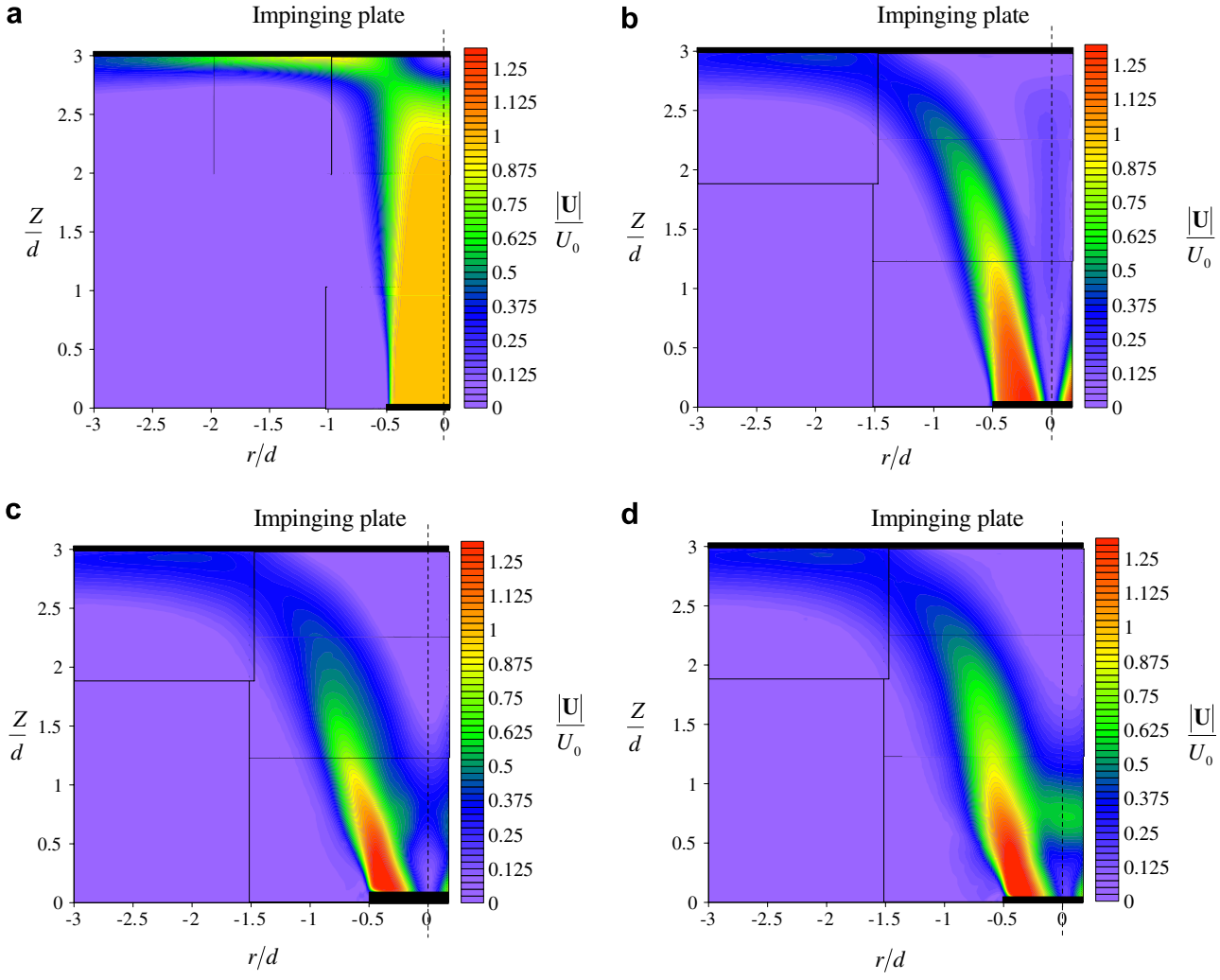

Fig. 7. Distributions of the normalized absolute mean velocity in the impinging jets. (a) $S = 0$; (b) $S = 0.41$; (c) $S = 0.70$ and (d) $S = 1.0$.

Hereafter, the cases with $S = 0.41$, $S = 0.70$, and $S = 1.0$ will be referred to as flows with low, intermediate, and high swirl rates, respectively.

In Figs. 6–12, spatial distributions of the mean velocity, second-, and third-order moments of velocity fluctuations are presented. No data smoothing or approximation was performed. It must be underlined that r/d is mainly negative in the plots (that is not typical of the cylindrical coordinate system), therefore the statistical moments are presented in consideration of the following conditions: $v(r) = -v(-r)$, $w(r) = -w(-r)$, $u(r) = u(-r)$. Fig. 6 shows the spatial distributions of the normalized axial component of mean velocity. For the conventional impinging jet, the potential core is observed up to $z = 2d$ from the nozzle exit. For the swirling flows, a maximal value of the axial velocity was found to be larger than the mean flow rate velocity U_0, and a significantly greater spreading rate was observed. For the jet at the low swirl rate of $S = 0.41$, a peculiarity was found in the lengthy recirculation zone characterized by the negative value of the axial mean velocity. As can be seen from Fig. 6b, the recirculation zone develops directly from the impinging plate towards the nozzle exit. The axial velocity at the jet centerline maintains an almost constant small negative value in the range of $z/d = 0.5$–2.5. A similar behavior was reported by Nozaki et al. (2003) for the swirling impinging jet with $Re = 4{,}000$, $H/d = 2$ and $S = 0.43$. For the impinging jet flows at intermediate and high swirl rates, the size of the recirculation zone is smaller (Fig. 6c and d) and the axial velocity has a minimum at about $z = 0.7d$ from the nozzle exit. The spatial distributions of normalized mean velocity are presented in Fig. 7. For the conventional impinging jet, the magnitude of the mean velocity is significantly higher near the impinging plate as compared to the swirling jet cases. Similarly to the axial mean velocity distributions, the absolute velocity patterns are congruent for the flows with intermediate and high swirling rates. For all swirling jet cases, the value of the absolute mean velocity rapidly decays downstream in contrast to the non-swirling impinging jet. Similar behavior was also reported by Abrantes and Azevedo (2006). The spatial distributions of the radial and axial components of the turbulent kinetic energy (TKE) are presented in

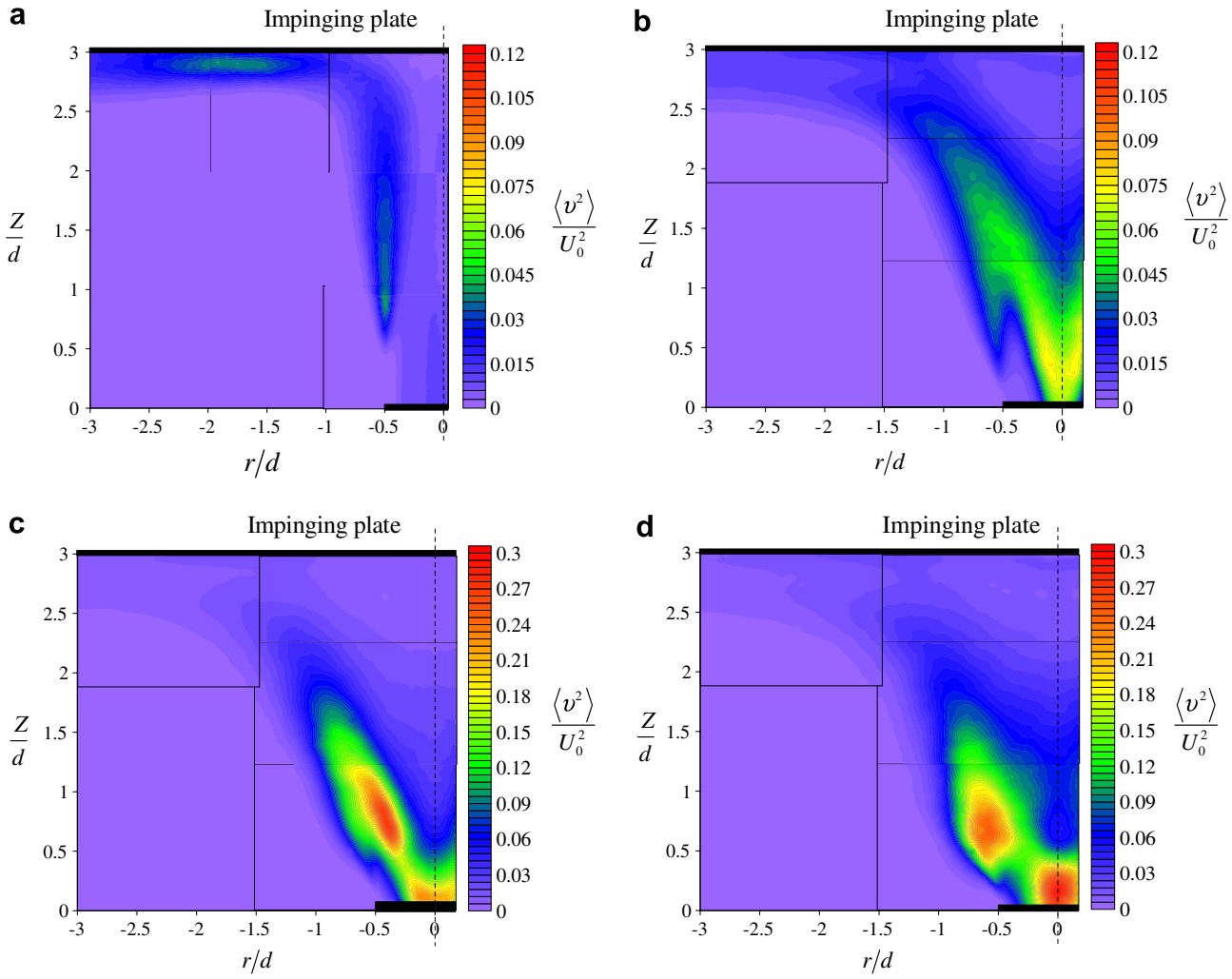

Fig. 8. Distributions of the normalized radial component of the turbulent kinetic energy in the impinging jets. (a) $S = 0$; (b) $S = 0.41$; (c) $S = 0.70$ and (d) $S = 1.0$.

Figs. 8 and 9, respectively. For conventional jet flow, the highest values of $\langle v^2 \rangle$ and $\langle u^2 \rangle$ correspond to the mixing layer, and maximum of the streamwise component of the TKE is greater than those for the transversal component $\langle v^2 \rangle$. For the low swirl rate, the distributions of the TKE components have high magnitudes in the area of the inner mixing layer, and they reach their maximum values close to the nozzle exit. For the flows at $S = 0.70$ and $S = 1.0$, the maximum values of the TKE components are significantly higher in comparison to the flows at $S = 0$ and $S = 0.41$. The local maxima of $\langle v^2 \rangle$ are observed directly in the vicinity of the nozzle exit and in the region near $z = 0.7d$ and $r = 0.5d$, while $\langle u^2 \rangle$ reaches its maximum at the edge of the recirculation zone.

Distributions of the Reynolds stress $\langle uv \rangle$ are presented in Fig. 10. In Figs. 10c and d, the color scale contains a rainbow interval which has the same values used in Fig. 10a and b to allow direct comparison with the $S = 0$ and $S = 0.41$ cases in the range of $z/d > 1$. The edges of the color scale are extended by sky blue and pink colors in order to cover the significantly higher values for $S = 0.70$ and $S = 1.0$ in the interval of $z/d < 1$. Near the impinging plate, the magnitudes of the Reynolds stress $\langle uv \rangle$ are significantly higher for the conventional jet as compared to the swirling jet cases. For the cases with intermediate and high swirl rates (Figs. 10c and d), $\langle uv \rangle$ reaches a significantly high magnitude near the nozzle exit (about 5 times higher than for the $S = 0$ and $S = 0.41$ cases, as can be seen from the color scale). Spatial distributions of the third-order moments $\langle u^2 v \rangle$ and $\langle u^3 \rangle$ are presented in Figs. 11 and 12, respectively. Similarly to the off-diagonal Reynolds stresses, the color bar for the $S = 0.71$ and $S = 1.0$ cases is extended, and its core coincides with the bars for the cases $S = 0$ and $S = 0.41$. For $S = 0$, the distribution of $\langle u^2 v \rangle$ has areas of negative and positive values in the jet mixing layer, where the positive value is closer to the jet core. From Fig. 11b, it can be seen that the distributions of $\langle u^2 v \rangle$ for $S = 0.41$ have a more complicated sign-alternating structure and contain two zones of positive and two zones of negative values in the mixing layers. Concerning cases with intermediate and high swirl rates, especially near the nozzle exit, a significant difference between the

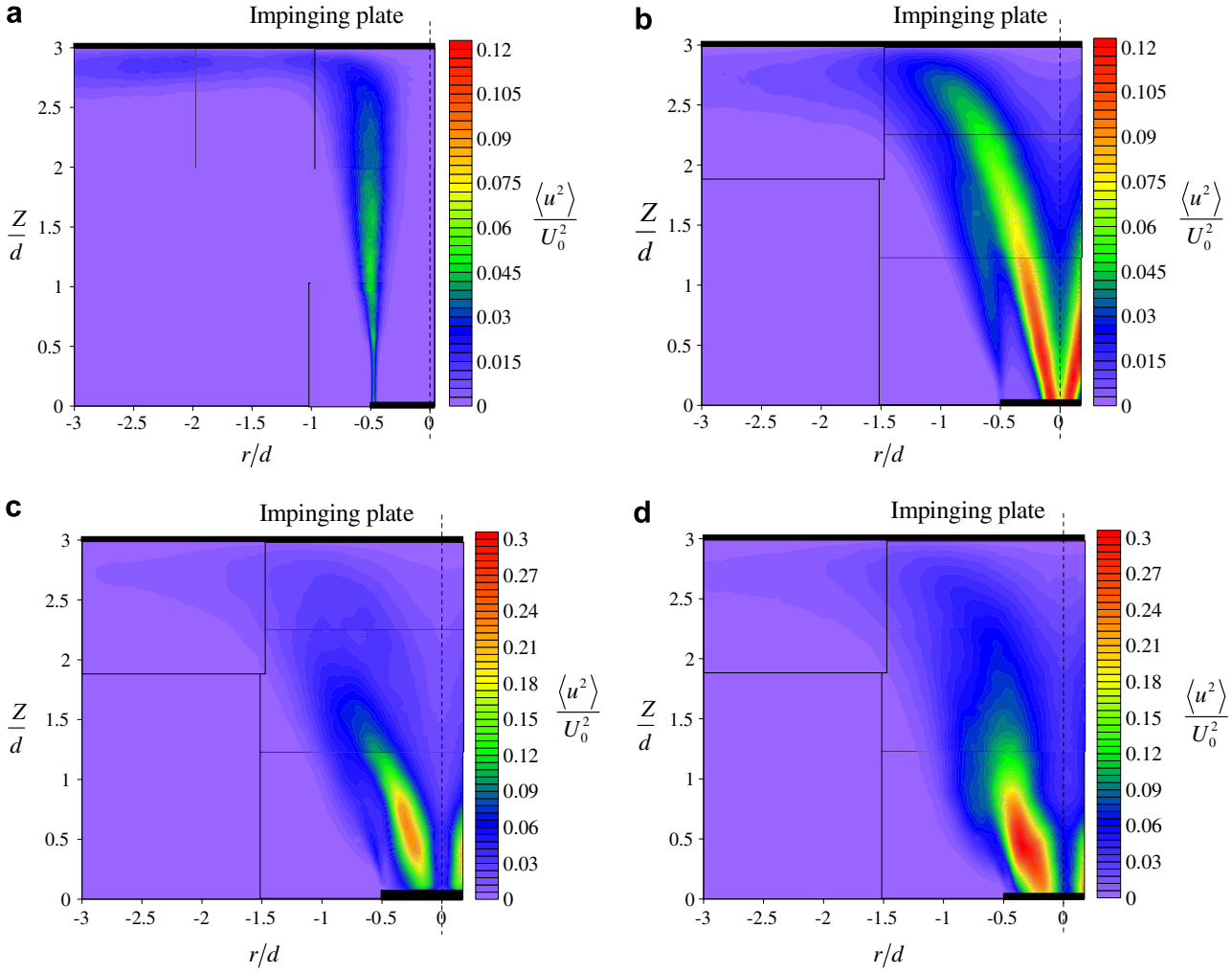

Fig. 9. Distributions of the normalized axial component of the turbulent kinetic energy in the impinging jets. (a) $S = 0$; (b) $S = 0.41$; (c) $S = 0.70$ and (d) $S = 1.0$.

distributions is found. For the $S = 1.0$ case, a region of large positive values of $\langle u^2 v \rangle$ is observed near the jet axis, and a region of negative values is seen for $r/d < 0.4$. Additionally, a distinct positive peak is found near $z/d = 0.3$ and $r/d = 0.5$. In the case of the intermediate swirl rate, the distribution of $\langle u^2 v \rangle$ is much more complicated near the recirculation zone. Thus, significant negative values are observed close to the nozzle exit at $r/d \approx 0.2$. Similar to the $S = 1.0$ case, a large zone of negative values of $\langle u^2 v \rangle$ is observed. Analyzing the spatial distribution of the axial flux $\langle u^3 \rangle$ of the axial component of the turbulent kinetic energy (Fig. 12) for the $S = 0$ cases extensive zones of positive and negative values are observed in the jet mixing layer, where the negative zone is closer to the jet axis. For the $S = 0.41$ case, a large area of positive values of $\langle u^3 \rangle$ is located in the recirculation bubble, bounded by a lengthy area of negative values. For the $S = 0.70$ and $S = 1.0$ cases, the distributions of $\langle u^3 \rangle$ are more complicated than those in the $S = 0$ and $S = 0.41$ cases. Extensive areas of large negative values are situated around the recirculation bubble. For the jet at $S = 1.0$, a large area with positive values of $\langle u^3 \rangle$ is observed close to the jet axis for $z/d > 0.3$. In summary, the distributions of the statistical moments (especially of the third-order moments) substantially differ with swirl rate variation, especially for flow regimes with vortex breakdown.

In Figs. 13–17, the distributions of the axial and radial components of mean velocity and several second- and third-order moments are presented for the $z = 2d$ cross-section (one diameter from the impinging plate). Together with the spatial distributions discussed above, these plots show the evolution of the moments with increasing swirl number and can give additional quantitative information, which will be used during the estimation of the terms of balance equations. All presented profiles are the approximations of experimental data by fit functions. As an example, raw experimental points are shown in Figs. 15b and 17a in order to demonstrate the data scatter. Hereafter, the cases with $S = 0$ (case with the highest spatial resolution), $S = 0.41$, and $S = 1.0$ are considered as the most representative. Thus, results for the $S = 0.70$ case are only presented in Figs. 13a, 15a and b, 16a and b in order to

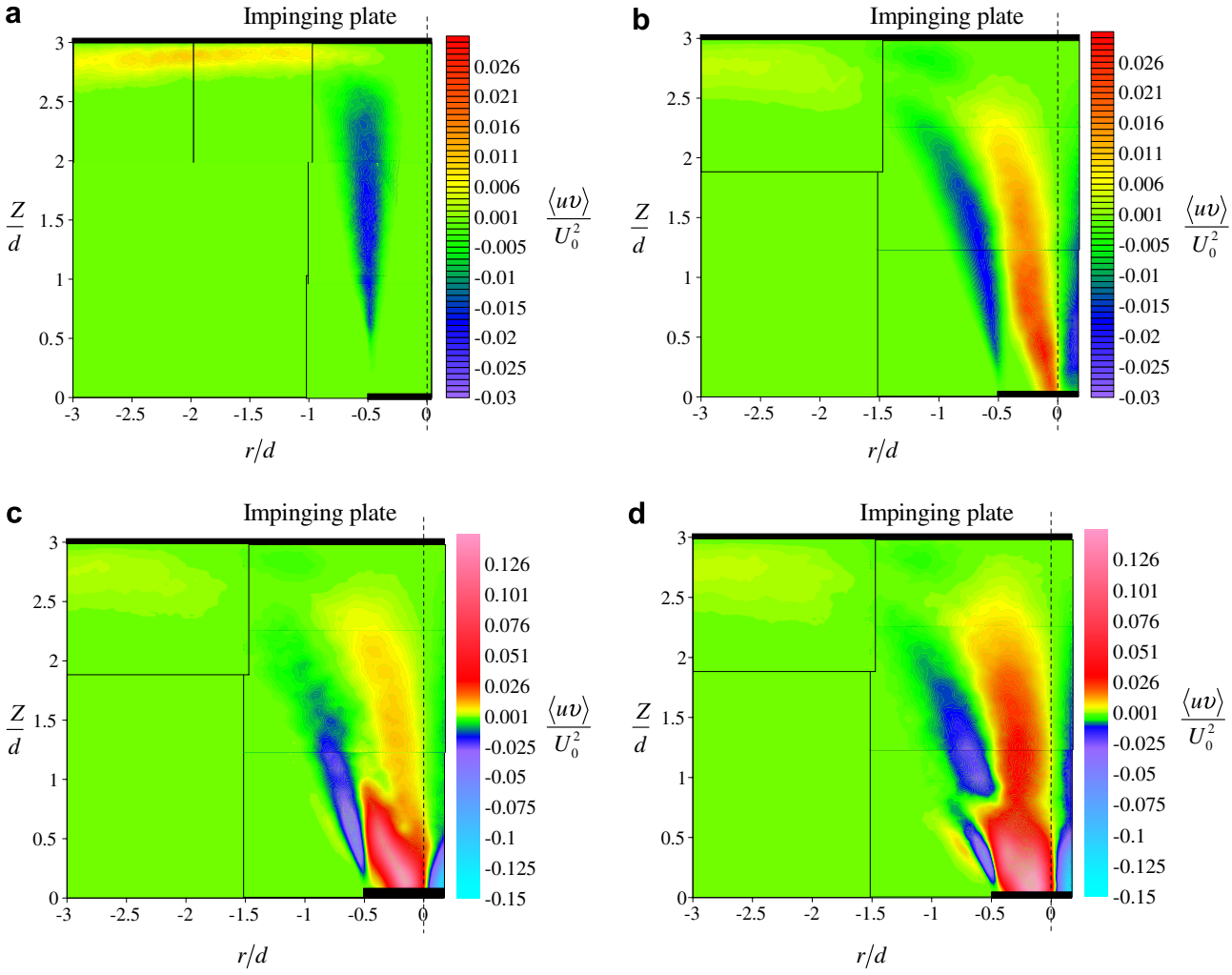

Fig. 10. Distributions of the normalized Reynolds stress in the impinging jets. (a) $S = 0$; (b) $S = 0.41$; (c) $S = 0.70$ and (d) $S = 1.0$.

precisely demonstrate the flow structure evolution. Note that the case with $S = 0.70$ can be described as a transitional state between low and high swirl rate cases, and thus the distributions of the moments often demonstrate non-monotonous behavior. For the swirling jets, the axial component of the mean velocity (Fig. 13a) significantly differs from the conventional jet case and has a negative value at the jet axis because of the presence of the recirculation zone. Variations of the radial component of the mean velocity across the jets are presented in Fig. 13b. For the swirling jets, a radial velocity several times higher in magnitude is observed which corresponds to a significantly greater spreading rate.

For the distributions of Reynolds stress $\langle uv \rangle$ (Fig. 14), when the swirl is introduced, the local minimum appears in the region of $r/d = 0.5$, and the location of the maximum shifts to larger values of r with the growth of S. For the selected cross-section, the shapes of the radial and axial TKE component distributions are similar for all cases and have an off-axis maximum (see Fig. 15), except in the $S = 0.70$ case, where two local maxima of $\langle u^2 \rangle$ are observed. It should be noted that for swirling jets, the value of $\langle v^2 \rangle$ reaches its maximum in the outer mixing layer, whereas for $\langle u^2 \rangle$, the location of the maximum corresponds to the inner layer (except of $S = 0.70$ case). In general, the profiles of the radial and axial components of the TKE become higher and wider with increased swirl rate. Variations of the third-order moments of fluctuating velocity across the jet are presented in Figs. 16 and 17. For $\langle v^3 \rangle$, corresponding to the radial flux of the radial component of the TKE, the swirl leads to a maximum several times higher in value than in the outer mixing layer. In contrast to the presented radial fluxes, the axial fluxes $\langle u^3 \rangle$ and $\langle uv^2 \rangle$ for $S = 0.41$ and $S = 1.0$ become positive in the near axis region corresponding to the recirculation zone. Comparing the $S = 0.41$ and $S = 0.70$ cases, it can be concluded that for the second one the distribution of $\langle v^3 \rangle$ is closer to the $S = 1.0$ case. However, the difference between the distributions of $\langle u^3 \rangle$ for the $S = 1.0$ and $S = 0.70$ cases is greater than the difference for the $S = 1.0$ and $S = 0.41$ cases (Fig. 16b).

In order to demonstrate the evolution of the second and third order moments with z/d, the distributions of $\langle v^2 \rangle$, $\langle u^2 \rangle$ and $\langle u^3 \rangle$ for the $S = 0.41$ and $S = 1.0$ cases are

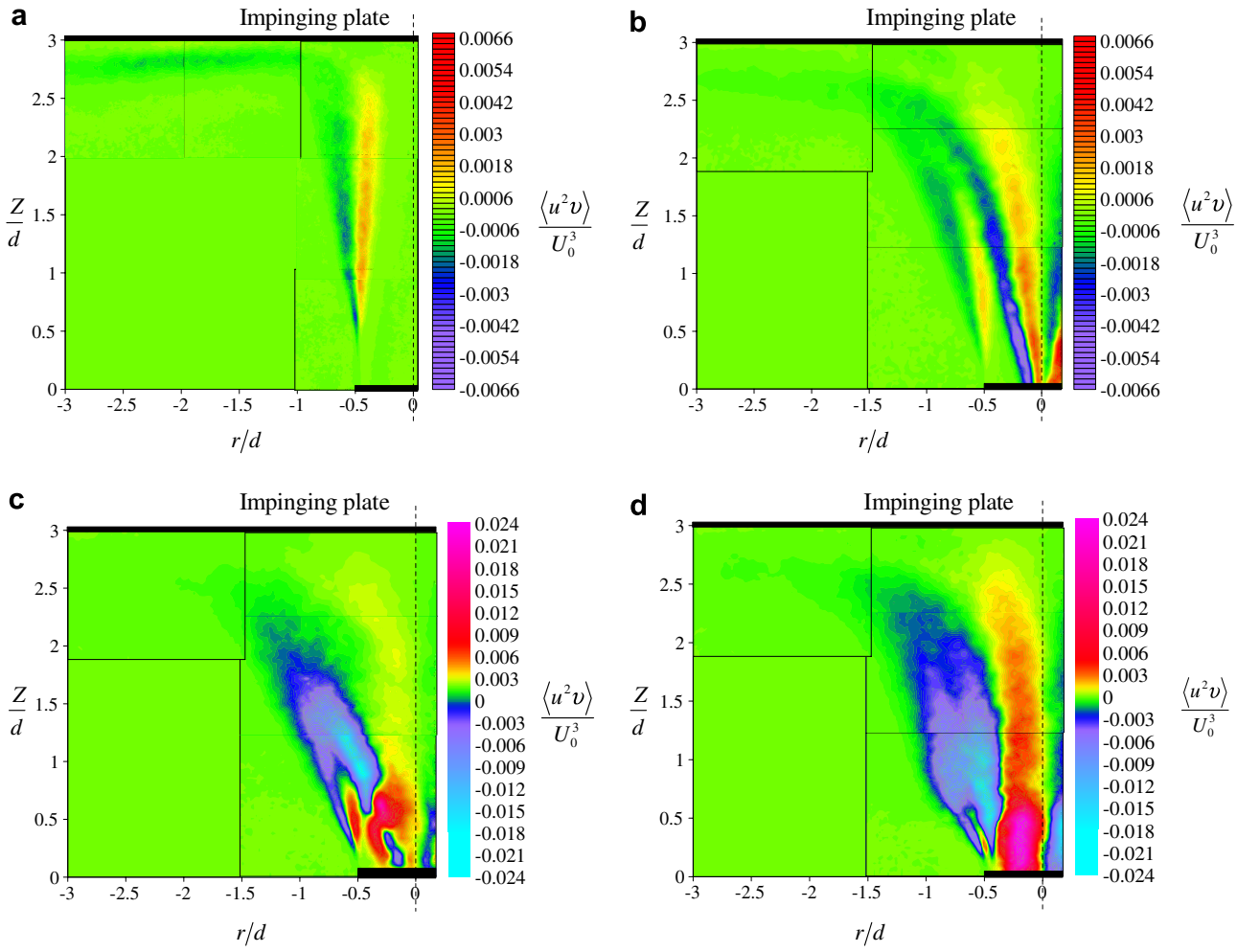

Fig. 11. Distributions of the normalized radial flux of the axial component of the turbulent kinetic energy in the impinging jets. (a) $S = 0$; (b) $S = 0.41$; (c) $S = 0.70$ and (d) $S = 1.0$.

presented in Figs. 18–20 for $z/d = \{0.5; 1.0; 1.5; 2.0\}$ cross-sections. Concerning the $S = 0.41$ case, distributions of the TKE components decrease monotonously with z/d, and a decay of the second local maximum takes place. For the $S = 1.0$ case, the distributions of the TKE components become more smooth with the increase of z/d, and their magnitude decreases more rapidly (by 5 times) while z/d is changing from 0.5 to 2.0. Similarly to the second-order moments, the third-order moment $\langle u^3 \rangle$ (Fig. 20) becomes more smooth with z/d growth, and its magnitude decreases monotonously in the case of a low swirl rate ($S = 0.41$, Fig. 20a). For the impinging jet flow at $S = 1.0$, the magnitude of $\langle u^3 \rangle$ decays several times for the range $0.5 < z/d < 1.0$, whereas in the $z/d = 1.5$ and 2.0 cross-sections, the distributions of $\langle u^3 \rangle$ are very similar.

During the conventional impinging jet study, the standard 2D2C PIV technique was used instead of the Stereo PIV. Therefore, the azimuthal component of TKE $\langle w^2 \rangle$ was not measured, and neither were the non-zero third-order moments $\langle uw^2 \rangle$ and $\langle vw^2 \rangle$ corresponding to the $\langle w^2 \rangle$ fluxes. The second-order moment $\langle w^2 \rangle$ appeared in the convection, viscous diffusion, and production terms of the TKE budget Eq. (3), while the third order-moments contribute to turbulent diffusion. In the work of Nishino et al. (1996), where the axisymmetric impinging jet was studied by PTV, the authors reported that intensities of axial and radial velocity fluctuations were almost identical for the distance from the impinging plate less than $1.5d$. They also stated that the assumptions of $\langle uw^2 \rangle \approx \langle uv^2 \rangle$ and $\langle vw^2 \rangle \approx \langle v^3 \rangle$ were appropriate for the round impinging jet flow. The last relation was also used by Panchapakesan and Lumley (1993) during their estimation of the TKE budget in the free round jet. Later, Bogey and Bailly (2005) demonstrated that the assumption of $\langle vw^2 \rangle \approx 0.5\langle v^3 \rangle$ was more appropriate for a free turbulent jet. Fig. 21 demonstrates the comparison of the distributions of third-order moments $\langle v^3 \rangle$ and $\langle vw^2 \rangle$ obtained by Nishino et al. (1996), with the experimental points approximated by the curves. It is clearly seen that the last assumption is more appropriate. Hereinafter, during the estimation of the TKE budget for conventional impinging jet flow, the following assumptions will be used: $\langle vw^2 \rangle \approx 0.5\langle v^3 \rangle, \langle uw^2 \rangle \approx \langle uv^2 \rangle$ and $\langle w^2 \rangle \approx \langle v^2 \rangle$.

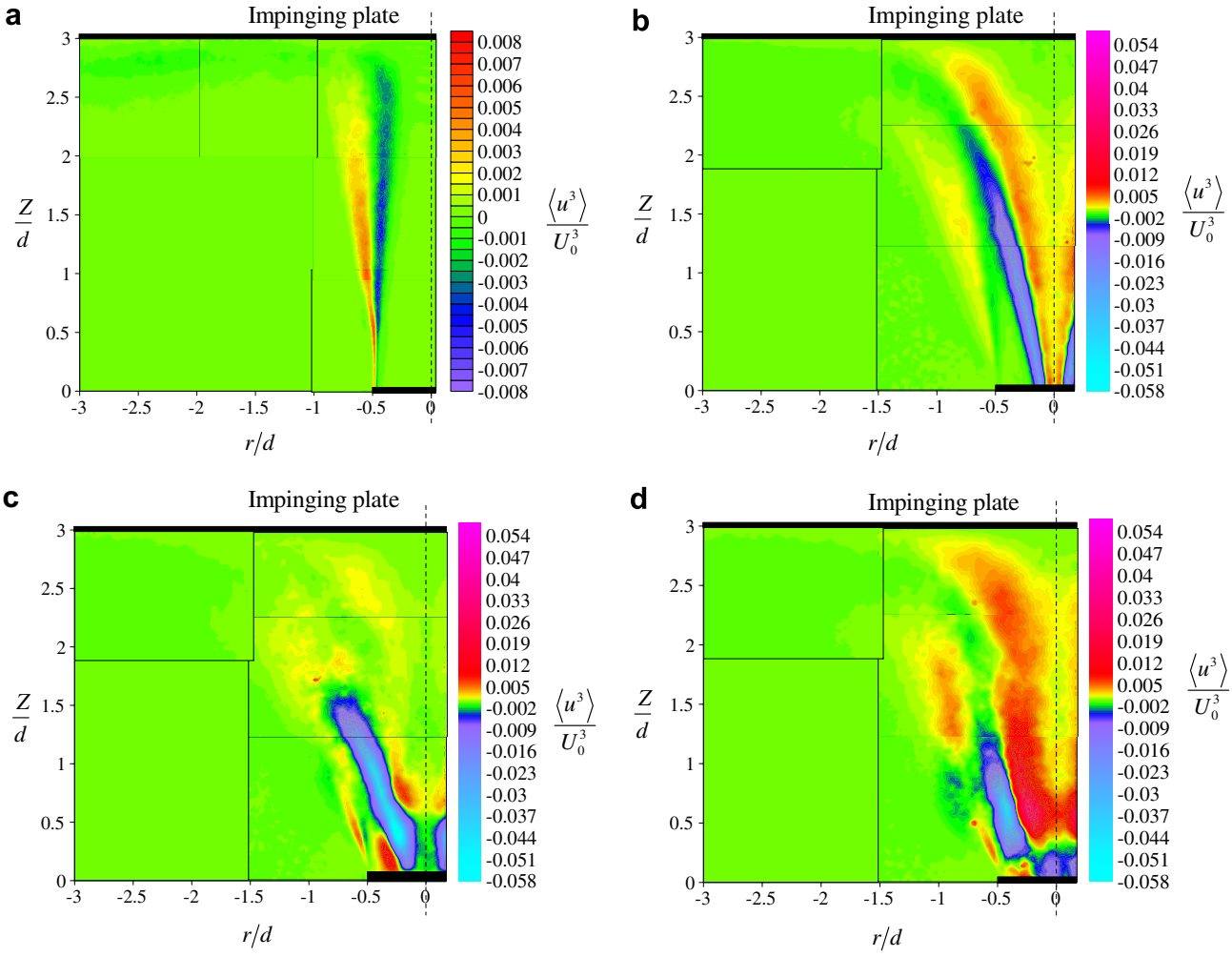

Fig. 12. Distributions of the normalized axial flux of the axial component of the turbulent kinetic energy in the impinging jets. (a) $S = 0$; (b) $S = 0.41$; (c) $S = 0.70$ and (d) $S = 1.0$.

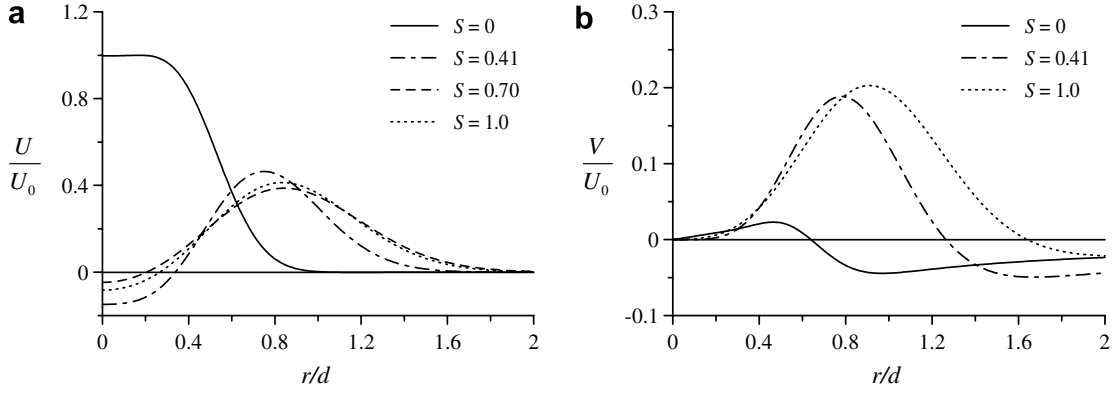

Fig. 13. Distributions of the axial (a) and radial (b) mean velocity across the impinging jets, $z/d = 2$.

3.3. Spatial resolution

When high-*Re*-number flows are studied experimentally, the limited spatial resolution of any experimental technique affects the magnitude of the measured second- and third-order moments, especially of the estimated dissipation rate. In this section, the effect of the PIV spatial resolution on the error of these quantities estimation is studied experimentally for the tested impinging jet configuration. Additionally, comparison with inexact theoretical analysis is performed. According to Willert and Gharib (1991) and Foucaut et al. (2004), the highest resolved wavenumber for PIV is determined by the interrogation area size Δ and can be found as $k_{max} = \pi/\Delta$. To analyze the influence

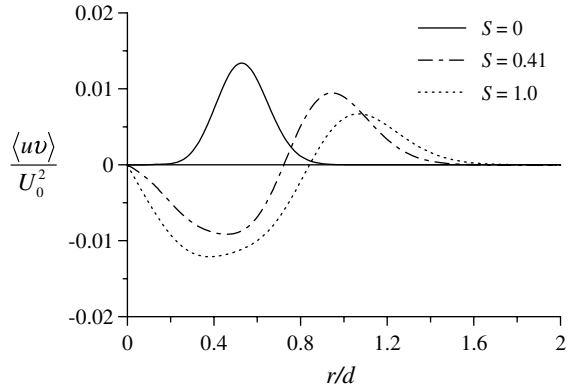

Fig. 14. Distributions of the Reynolds stress across the impinging jets, $z/d = 2$.

of the spatial resolution, Helland's model (6) is considered for the three-dimensional energy spectrum function (Ewing and George, 1994), which is similar to Pao's spectrum (7) for high wavenumbers. Further, the condition of homogenous isotropic turbulence is used.

$$E(k) = \alpha\varepsilon^{2/3}(L)^{5/3}\frac{(kL)^4}{(1+(kL)^2)^{17/6}}\exp\left(-\beta\frac{3}{2}(k\eta)^{4/3}\right) \quad (6)$$

$$E(k) = \alpha\varepsilon^{2/3}k^{-5/3}\exp\left(-\alpha\frac{3}{2}(k\eta)^{4/3}\right) \quad (7)$$

Here, the parameter $\alpha = 1.6$, β is taken to be equal to α, L is the integral lengthscale and η is the Kolmogorov lengthscale, which can be estimated as follows: $\eta = (\nu^3/\varepsilon)^{1/4}$. The following relation was used to estimate the integral lengthscale: $L \approx u'^3/\varepsilon$, where $u'^2 = \langle v^2 + w^2 + u^2\rangle/3$. In order to evaluate the lengthscales for the conventional impinging jet flow, the magnitude of the dissipation rate ε was assumed to be of the order of the production term in the TKE budget equation. Considering the transfer function of PIV as a sharp cut-off filter with the highest resolved wavenumber $k_{\max}$, the analytical ratios between the magnitudes of the estimated and true statistical characteristics are as follows:

$$f_{q^2}(k_{\max}) = \frac{q^2_{\text{meas}}}{q^2_{\text{true}}}(k_{\max}) = \int_0^{k_{\max}} E(k')\,dk' \Big/ \int_0^{\infty} E(k')\,dk' \quad (8)$$

$$f_{q^3}(k_{\max}) = \frac{q^3_{\text{meas}}}{q^3_{\text{true}}}(k_{\max}) = \int_0^{k_{\max}} W(k')\,dk' \Big/ \int_0^{\infty} W(k')\,dk' \quad (9)$$

$$f_{\varepsilon}(k_{\max}) = \frac{\varepsilon_{\text{meas}}}{\varepsilon_{\text{true}}}(k_{\max}) = \int_0^{k_{\max}} D(k')\,dk' \Big/ \int_0^{\infty} D(k')\,dk' \quad (10)$$

Here, $W(k) = -\nu k E(k)$, $D(k) = 2\nu k^2 E(k)$ and in terms of the used functions; $q^3 = \langle u^2 v + u^2 w + uv^2 + v^2 w + uw^2 + vw^2\rangle$, $q^2 = \langle v^2 + w^2 + u^2\rangle$. Complete derivation of these relations can be found in Alekseenko et al. (submitted for publication). For Pao's spectrum model, an analytical

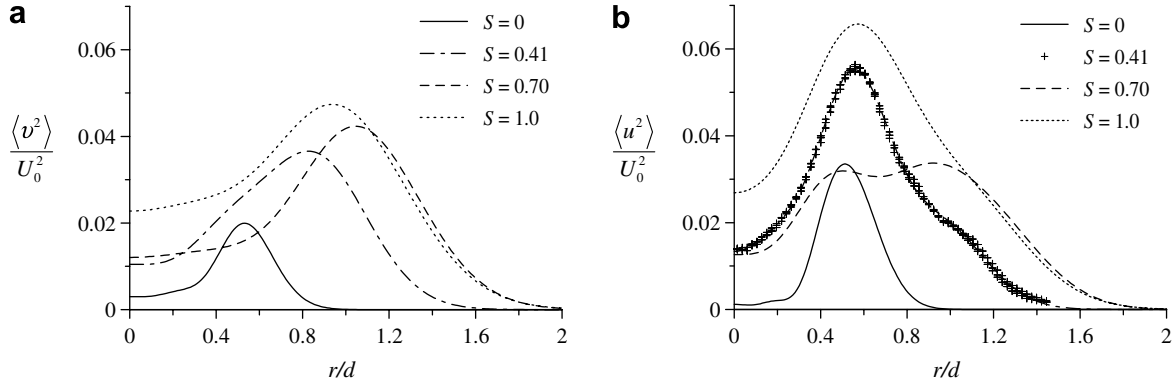

Fig. 15. Distributions of the radial (a) and axial (b) components the turbulent kinetic energy across the impinging jets, $z/d = 2$.

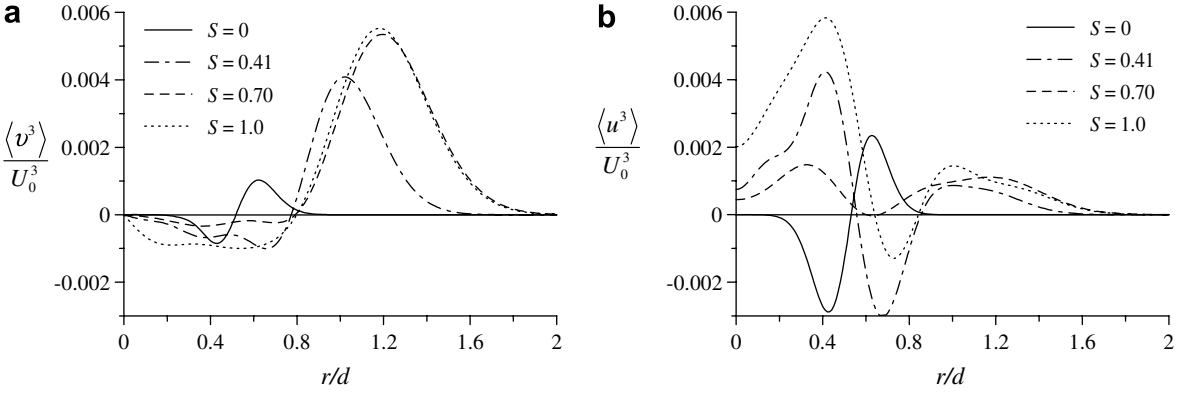

Fig. 16. Distributions of the third-order moments of the fluctuating velocity across the impinging jets, $z/d = 2$.

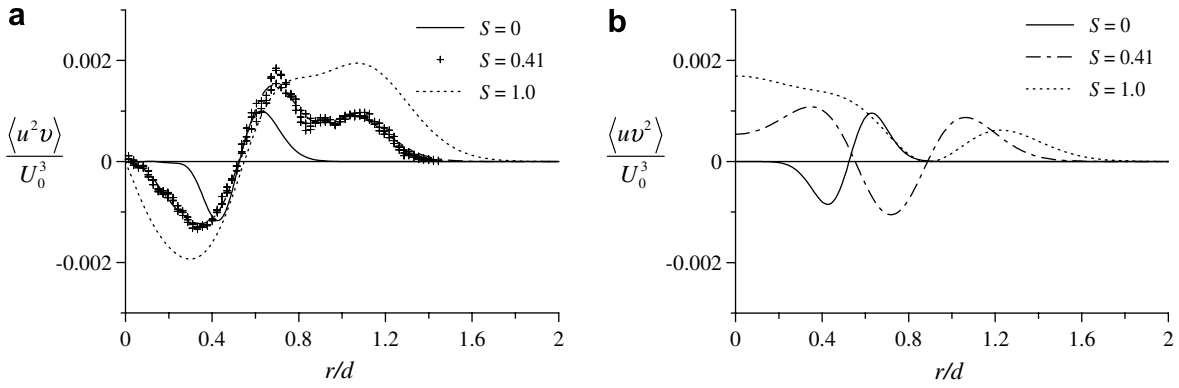

Fig. 17. Distributions of the mixed third-order moments of the fluctuating velocity across the impinging jets, $z/d = 2$.

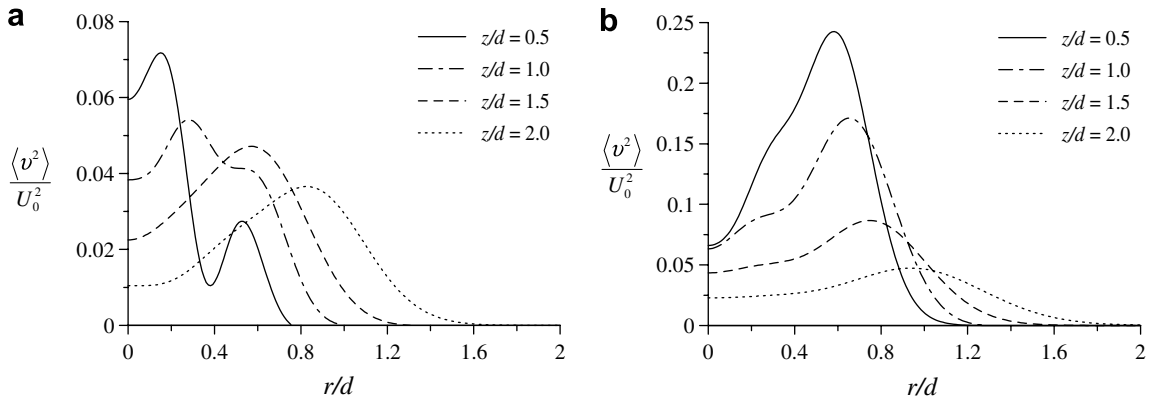

Fig. 18. Distributions of the radial component of the turbulent kinetic energy in the various cross-sections of the impinging jets. (a) $S = 0.41$; (b) $S = 1.0$.

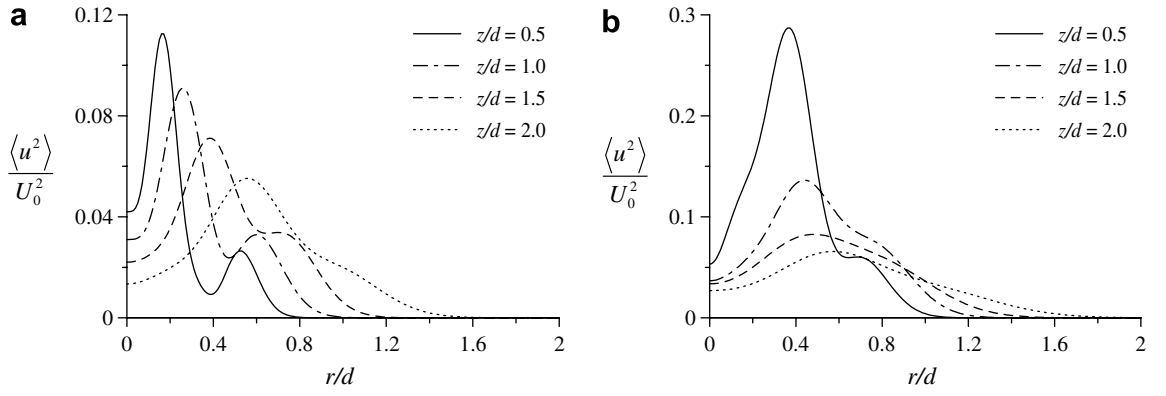

Fig. 19. Distributions of the axial component of the turbulent kinetic energy in the various cross-sections of the impinging jets. (a) $S = 0.41$; (b) $S = 1.0$.

expression (11) of the dissipation underestimation (scaling) coefficient (10) can be obtained.

$$f_\varepsilon = 1 - \exp\left(-\frac{3}{2}\alpha(k_{\max}\eta)^{4/3}\right) = 1 - \exp\left(-\frac{3}{2}\alpha(\pi\eta/\Delta)^{4/3}\right) \quad (11)$$

In Fig. 22a, the underestimation coefficients of dissipation in the case of the conventional impinging jet are presented for the different spatial resolution tested. The coefficient values are compared with prediction by (11) and with the fit function (12) reported by Alekseenko et al. (submitted for publication).

$$f_\varepsilon = 1 - \exp\left(-\alpha\left(\frac{3}{2}\left(\frac{\pi\eta}{\Delta}\right)^{4/3} + \left(\frac{\pi\eta}{\Delta - 5.87\eta}\right)^{3.15}\right)\right), \quad \text{where} \quad \Delta > 5.87\eta \quad (12)$$

During the estimation of the correction coefficients for the impinging jet, $\varepsilon_{\text{meas}}$ was taken as equivalent to the maximum of the absolute magnitude of the dissipation

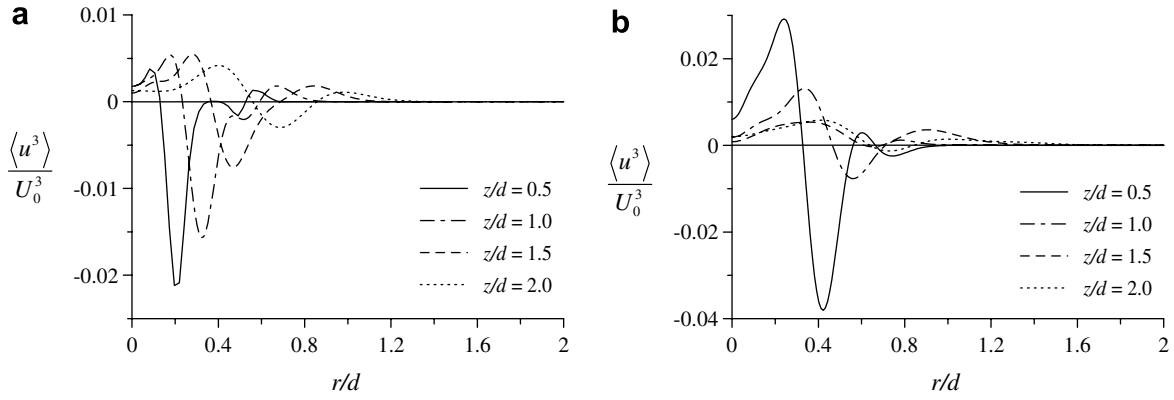

Fig. 20. Distributions of the axial flux of the axial component of the turbulent kinetic energy in the various cross-sections of the impinging jets. (a) $S = 0.41$; (b) $S = 1.0$.

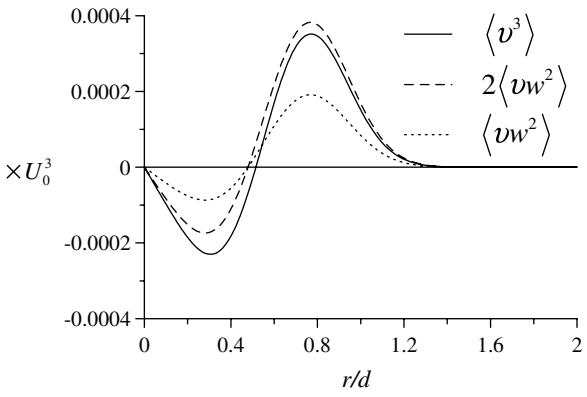

Fig. 21. Comparison of the third-order moments distributions across impinging jets reported by Nishino et al. (1996): $Re = 10{,}400$, $H/d = 5.86$, $z/d = 4.35$, $S = 0$.

calculated using (5) (see Fig. 23b) at the studied cross-section $z = 2d$. The value of $\varepsilon_{\text{true}}$ was found in the following iterative way. At the first stage f_ε was taken to be equal to unity and approximate value of η was found from $\eta = (v^3 f_\varepsilon/\varepsilon_{\text{meas}})^{1/4}$. At the next steps f_ε was estimated from (12) and then η was recalculated. Typically, for the cases with low spatial resolution (i.e. cases with $\Delta = 0.79$ and 0.52 in Table 1), about five iterations are enough for a good convergence. In the case of the highest spatial resolution, second iteration predicted $f_\varepsilon = 1$ as it was assumed at the first one. For all cases of spatial resolution, the estimated value of $\varepsilon_{\text{true}}$ was found to be close to each other and to the maximum value of the production term. The obtained final values of f_ε are in good agreement with the measurements in the free jet at Re 25,000 by Alekseenko et al. (submitted for publication), and they similarly show a faster growth of the correction coefficient at high wavenumbers ($\Delta/\eta < 15$) compared to Pao's model function. In spite of the restrictive conditions used (i.e. local isotropy assumption, model spectrum that is expected to significantly differ from the real one) for sufficiently non-homogenous impinging jet flow, the chosen approach is found to be applicable for the range of $10 < \Delta/\eta \leqslant 20$. This can be explained by the fact that fluctuations at high wavenumbers, where the energy is mostly dissipated, tend to be isotropic due to the energy transfer mechanism that erases information about mean flow properties. Thus, for high Re flows, micro-scale fluctuations are expected to obey the locally isotropic turbulence regularities. In Table 1, the spatial resolutions and the correction coefficients by (12) for the present set of measurements are listed. Helland's spectrum model was used to

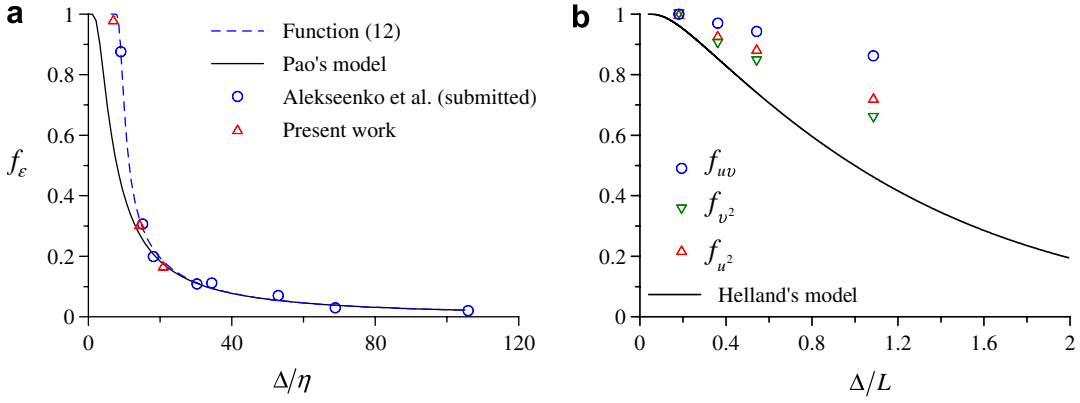

Fig. 22. The underestimation coefficients for dissipation (a) and for the second-order moments (b) together with the corresponding theoretical predictions. $S = 0$; $z/d = 2$.

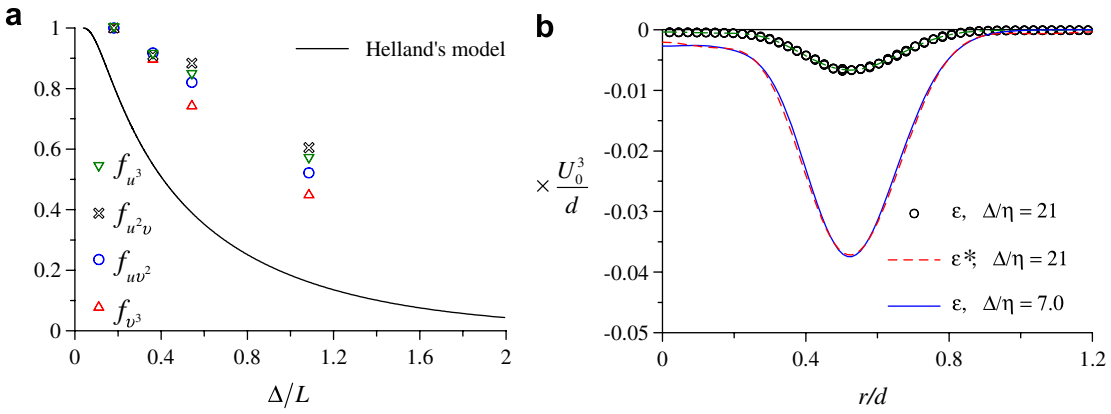

Fig. 23. The underestimation coefficients for the third-order moments (a) and theoretical prediction. Example of dissipation correction assessment (b) for the non-swirling impinging jet. $S = 0$; $z/d = 2$.

determine the underestimation coefficient of the TKE. In Fig. 22b, the underestimation coefficient (8) is plotted along with the experimental points for the second-order moments. During the estimation of correction coefficients, the absolute maximum values of the profiles (see Figs. 14 and 15) were used. The data with the highest spatial resolutions were considered to be true. The ratio $L = 40\eta$ was found for the considered cross-section of the non-swirling jet, and function (8) was calculated numerically. The underestimation coefficients for the third-order moments are presented in Fig. 23a. Similarly to the second-order moments, the absolute maximum and minimum values of the triple moments (see Figs. 16 and 17) were used for the estimation of experimental points and the values for the case with the highest spatial resolution were considered to be true. A significant difference is observed, indicating that the use of the isotropy assumption and the model spectrum is unsuitable for prediction of the second- and third-order moment underestimations. Nevertheless, the theoretical prediction and the experimental data of the conventional jet study with different spatial resolution demonstrates that the error of second- and third-order moment estimations are higher than 20% and 40%, respectively, if $\Delta/L > 1$ and is significantly higher for the dissipation rate.

For the studied swirling impinging jet flows, the ratio of the integral and Kolmogorov lengthscales is equal to about 135 at $z/d = 2$ cross-section, leading to the following relation: $\Delta/L \approx 0.1$. According to the prediction by Helland's spectrum model for $L/\eta = 135$, this order of spatial resolution leads to an underestimation error less than 5% and 10% for the second- and third-order moments, respectively. However, the dissipation rate is significantly underresolved for the tested swirling jet cases, for which the spatial resolution was around $\Delta/\eta \approx 14$ (see Table 1). Thus, for the swirling jets, the TKE dissipation rate was found using (5) and was then scaled by the underestimation coefficient (12) in the following way:

$$\varepsilon* = \varepsilon_{\text{meas}}/f_\varepsilon \tag{13}$$

The values of scaling coefficients estimated by using the iterative procedure described above are presented in Table 1. The example of dissipation scaling for the conventional impinging jet at the studied cross-section is presented in Fig. 23b. For the spatial resolution $\Delta/\eta = 20$, Eq. (12) predicts the scaling coefficient to be equal to $1/f_\varepsilon = 5.2$. For the highest spatial resolution, there is no need for the dissipation correction (see Table 1). It should be noted that the corrected profile (dashed line) is very close to the dissipation profile for the highest resolution (solid line) in the whole range of r/d. The next section presents the results of the estimation of the terms of the AMM and TKE balance equations.

3.4. Terms of conservation equations

For the studied impinging jets at $S = 0$, $S = 0.41$, and $S = 1.0$, all the terms of the AMM transport equation were obtained for the $z = 2d$ cross-section. The estimated terms are presented in Fig. 24. Transport by mean pressure was found as a residual term of the AMM transport equation. The viscous terms were found to be negligible in comparison to the others, and are therefore not plotted. For conventional jet flow, the convection term has an almost constant positive value near the jet axis. For the swirling impinging jets, convection has a positive peak at $r/d \approx 0.8$ where the maximum of the axial mean velocity is observed, and is rather small near the jet axis. In contrast to flow with $S = 0$, turbulent diffusion has a significantly greater magnitude for the swirling jet conditions, and it reaches a high positive value in the recirculation zone. An interesting peculiarity is observed for the swirling jets: turbulent diffusion is negative in the outer mixing layer, unlike the non-swirling jet case. In general, the term corresponding to transport by the mean pressure gradient becomes greater and its profile widens with an increased swirl rate.

All the terms of the TKE budget equation estimated for the $z = 2d$ cross-section of the studied impinging jets are presented in Fig. 25. The viscous diffusion term in the TKE budget was found to be negligible in comparison to the other terms. The dissipation term for the swirling jets

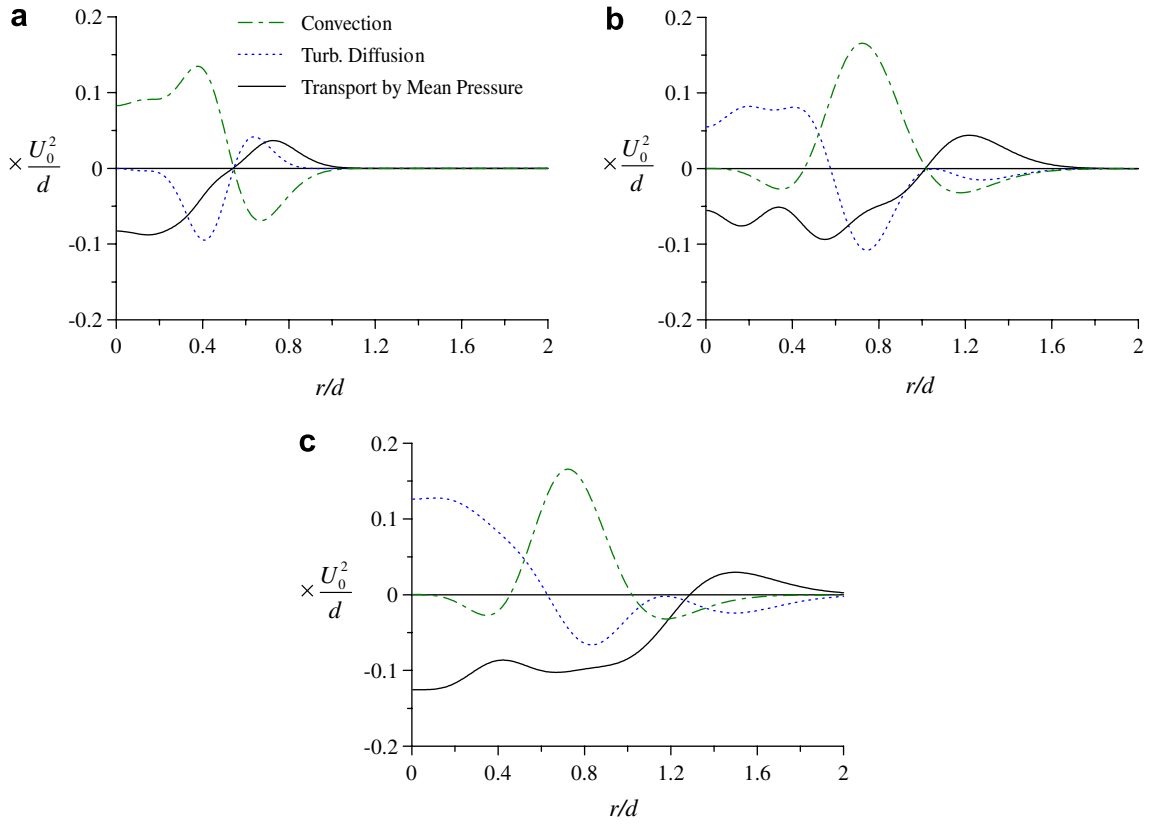

Fig. 24. The normalized terms of the axial mean momentum transport equation for the impinging jets, $z/d = 2$. (a) $S = 0$; (b) $S = 0.41$ and (c) $S = 1.0$.

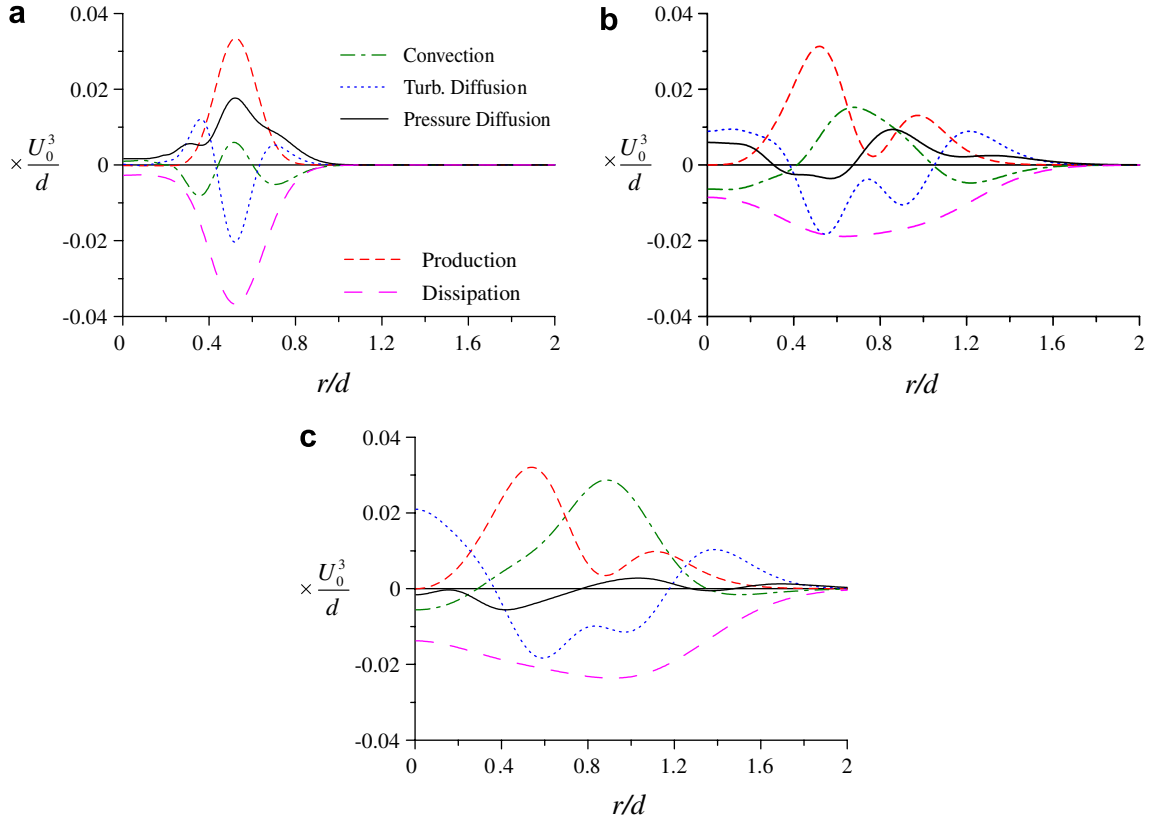

Fig. 25. The normalized terms of the turbulent kinetic energy budget equation for the impinging jets, $z/d = 2$. (a) $S = 0$; (b) $S = 0.41$ and (c) $S = 1.0$.

was estimated using correction procedure. Pressure diffusion was found as a residual term of the budget equation. In general, the same budget terms for the swirling impinging jets at $S = 0.41$ and $S = 1.0$ differ in shape, and for $S = 1.0$, they have a higher magnitude with the exception of the production and pressure diffusion terms. For the conventional impinging jet, the maximum magnitudes of dissipation, pressure diffusion and shear stress production are observed near $r/d \approx 0.5$, which corresponds to the mixing layer region. Two local maxima of the production term and two minima for turbulent diffusion are clearly seen for the swirling jets. The maxima of production correspond to the inner and outer mixing layers. Similarly to the AMM transport equation, turbulent diffusion has significant positive values near the jet axis. The dissipation term becomes significantly broader and has a lesser maximum absolute value when the swirl is applied. The convection term and turbulent diffusion are observed to have opposite signs throughout the whole tested cross-section. The pressure diffusion term has an alternating-sign form for swirling jets, and its magnitude decreases with the growth of swirl rate.

4. Conclusions

A swirling impinging turbulent jet at $Re = 8900$ was studied experimentally using the PIV and Stereo PIV techniques. The nozzle-to-plate distance was equal to three nozzle diameters, and the swirl rate S was varied from 0 to 1.0. Spatial distributions of the complete set of statistical moments (up to the third-order) of velocity fluctuations were measured for the studied flow conditions. Additionally, a special set of measurements was carried out to examine the contribution of limited PIV spatial resolution to the total measurement error. The error resulting from spatial averaging was analyzed from both the theoretical and experimental points of view.

By analyzing the spatial distributions of mean velocity, it was found that for the impinging jet at $S = 0.41$, a lengthy recirculation zone is located between the nozzle exit and the impinging plate. For the impinging jets at $S = 0.70$ and $S = 1.0$, a vortex breakdown was clearly observed and the recirculation zone was smaller ($0 < z/d < 1.5$). The vortex breakdown led to the intense generation of turbulence in the initial region of the jet and resulted to high values of the turbulence kinetic energy at the local regions, and hence to significantly large values of the third-order moments determining the turbulent diffusion of the energy. The Reynolds stress $\langle uv \rangle$ and third-order moments were observed to have about 5 times higher values in the region of vortex breakdown than in the rest of the flow domain, where the values are close to the $S = 0$ and $S = 0.41$ cases.

For the cross-section at one nozzle distance from the impinging wall, the terms of the axial mean momentum (AMM) transport equation were obtained for the jets at $S = 0$, 0.41, and 1.0. The terms of the AMM balance were found to be quite similar in shape for jets with swirl, but they significantly differ from the non-swirling jet case. The major distinctions are caused by the distributions of the mean flow velocity. All the terms of the turbulent kinetic energy budget (TKE) equation were obtained for the above mentioned cross-section, where the dissipation term was estimated from the ensemble of instantaneous velocity fields, thereby allowing pressure diffusion to be found as the residual term. In terms of the TKE budget, the non-swirling jet represents a sufficiently different case from the swirling jets, as in the non-swirling case, the significant values of the TKE balance terms are only in the mixing layer. As was shown for all jet cases, the production terms have local maxima in the mixing regions; the convection term and turbulent diffusion are observed to have opposite signs over the whole tested cross-section. The magnitude of the pressure diffusion term decreases with the growth of swirl rate.

Acknowledgement

This work was supported by the RAS and SB RAS integration research projects and by the RFBR foundation (grant N 07-08-00213).

References

Abrantes, J.K., Azevedo, L.F.A., 2006. Fluid Flow Characteristics of a Swirl Jet Impinging on a Flat Plate. In: Proceedings of the thirteenth International Symposium on Application of Laser Techniques to Fluid Mechanics, Lisbon, Portugal, June 26–29, 2006.

Alekseenko, S.V., Bilsky, A.V., Dulin, V.M., Markovich, D.M., Tokarev, M.P., submitted for publication. Stereo PIV measurements of turbulence characteristics in an axisymmetric jet. Exp. Fluids.

Alekseenko, S., Bilsky, A., Heinz, O., Ilyushin, B., Markovich, D., Vasechkin, V., 2002. Fine structure of the impinging turbulent jet. In: Rodi, W., Fueyo, N., (Eds.), Proceedings of the Fifth International Symposium on Engineering Turbulence Modeling and Experiments, Mallorca, Spain, September 16–18, 2002, pp. 597–606.

Alekseenko, S.V., Kuibin, P.A., Okulov, V.L., 2003. Introduction into Theory of Concentrated Vortices. Institute of Thermophysics, Novosibirsk, Nauka.

Alekseenko, S.V., Kuibin, P.A., Okulov, V.L., Shtork, S.I., 1999. Helical vortices in swirl flow. J. Fluid Mech. 382, 195–243.

Alekseenko, S.V., Markovich, D.M., Semenov, V.I., 1997. Effect of external disturbances on the impinging jet structure. In: Giot, M., Mayinger, F., Celata, G.P., (Eds.) Proceedings of the Fourth World Conference on Experimental Heat Transfer, Fluid Mech. and Thermodynamics, Brussels, Belgium, June 2–6, 1997, pp. 1815–1822.

Azevedo, L.F.A., Almeida, J.A., Duarte, L.G.C., 1997. Mass transfer to swirling impinging jets. In: Giot, M., Mayinger, F., Celata, G.P., (Eds.) Proceedings of the Fourth World Conference on Experimental Heat Transfer, Fluid Mech. and Thermodynamics, Brussels, June 2–6, 1997. 3, pp. 1759–1766.

Billant, P., Chomaz, J.-C., Huerre, P., 1998. Experimental study of vortex breakdown in swirling jets. J. Fluid Mech. 376, 183–219.

Bogey, C., Bailly, C., 2005. Computation of the self-similarity region of a turbulent round jet using large eddy simulation. In: Lamballais, E., Friedrich, R., Geurts, B.J., Metais, O., (Eds.) Proceedings of the Sixth International ERCOFTAC Workshop on Direct and Large Eddy Simulation, Poitiers, France, September 12–14, 2005.

Cooper, D., Jackson, D.C., Launder, B.E., Liao, G.X., 1993. Impinging jet studies for turbulence model assessment – I. Flow field experiments. Int. J. Heat Mass Transfer 36 (10), 2675–2684.

Didden, N., Ho, C.-M., 1985. Unsteady separation in a boundary layer produced by an impinging jet. J. Fluid Mech. 160, 235–256.

Donaldson, C., Snedeker, R., Margolis, A., 1971. A study of free jet impingement heat transfer. Part 2. Free jet turbulent structure and impingement heat transfer. J. Fluid Mech. 45, 477–512.

Ewing, D., George, W.K., 1994. Spatial attenuation of vorticity measurements by multi-wire probes. In: Fluid Measurements and Instrumentation. ASME Fluids Division Summer Meeting, Lake Tahoe, Nevada, June 19–23. FED-Vol. 183.

Foucaut, J.M., Carlier, J., Stanislas, M., 2000. Post-processing of PIV records to allow derivative computation. In: Proceedings of the tenth International Symposium on Application of Laser Techniques to Fluid Mechanics, Lisbon, Portugal, July 10–13, 2000.

Foucaut, J.M., Carlier, J., Stanislas, M., 2004. PIV optimization for the study of turbulent flow using spectral analysis. Meas. Sci. Tech. 15, 1046–1058.

Foucaut, J.M., Stanislas, M., 2002. Some considerations on the accuracy and frequency response of some derivative filters applied to particle image velocimetry vector fields. Meas. Sci. Technol. 13, 1058–1071.

Gardon, R., Akfirat, J., 1965. The role of turbulence in determining the heat transfer characteristics of impinging jets. Int. J. Heat Mass Transfer 8 (10), 1261–1272.

George, W.K., Hussein, H.J., 1991. Locally axisymmetric turbulence. J. Fluid Mech. 233, 1–23.

Gupta, A.K., Lilley, D.G., Syred, N., 1984. Swirl Flows. Abacus Press, Kent Engl.

Heinz, 0., Ilyushin, B., Markovich, D., 2004. Application of a PDF based method for the experimental statistical processing of experimental data. Int. J. Heat Fluid Flow 25, 864–874.

Huang, L., El-Genk, M.S., 1998. Heat transfer and flow visualization experiments of swirling, multi-channel, and conventional impinging jets. Int. J. Heat Mass Transfer 41, 583–600.

Kataoka, K., Suguro, M., Degawa, H., Maruo, K., Mihata, I., 1987. The effect of surface renewal due to large-scale eddies on jet impingement heat transfer. Int. J. Heat Mass Transfer 30 (3), 559–567.

Landreth, C.C., Adrian, R.J., 1990. Impingement of a low Reynolds number turbulent circular jet onto a flat plate at normal incidence. Exp. Fluids 9, 74–84.

Lawson, N.J., Wu, J., 1997. Three-dimensional particle image velocimetry: error analysis of stereoscopic techniques. Meas. Sci. Technol. 8, 894–900.

Liang, H., Maxworthy, T., 2005. An experimental investigation of swirling jets. J. Fluid Mech. 525, 115–159.

Liu, T., Sullivan, J.P., 1996. Heat transfer and flow structures in an excited circular impinging jet. Int. J. Heat Mass Transfer 39, 3695–3706.

Nishino, K., Samada, M., Kasuya, K., Torii, K., 1996. Turbulence statistics in the stagnation region of an axisymmetric impinging jet flow. Int. J. Heat Fluid Flow 17, 193–201.

Nozaki, A., Igarashi, Y., Hishida, K., 2003. Heat transfer mechanism of a swirling impinging jet in a stagnation region. Heat Transfer – Asian Research 32 (8), 663–673.

Owsenek, B.L., Cziesla, T., Mitra, N.K., Biswas, G., 1997. Numerical investigation of heat and mass transfer in impinging axial and radial jets with superimposed swirl. Int. J. Heat Mass Transfer 40, 141–147.

Panchapakesan, N.R., Lumley, J.L., 1993. Turbulence measurements in axisymmetric jets of air and helium. Part I. Air jet. J. Fluid Mech. 246, 197–223.

Piirto, M., Saarenrinne, P., Eloranta, H., Karvinen, R., 2003. Measuring turbulence energy with PIV in a backward-facing step flow. Exp. Fluids 35, 219–236.

Raffel, M., Willert, C., Kompenhans, J., 1998. Particle Image Velocimetry. A Practical Guide. Springer, Berlin.

Stanislas, M., Okamoto, K., Kahler, C.J., 2005. Main results of the second international PIV challenge. Exp. Fluids 39, 170–191.

Stanislas, M., Okamoto, K., Kähler, C.J., Westerweel J., in press. Main results of the third international PIV Challenge. Exp. Fluids.

Vejrazka, J., Tihon, J., Marty, Ph., Sobolik, V., 2005. Effect of an external excitation on the flow structure in a circular impinging jet. Phys. Fluids 17 (10), 105102.1–105102.14.

Volchkov, E.P., Lukashanov, V.V., Semenov, S.V., 1996. Heat transfer in an impact swirling jet. Heat Transfer Res. 27, 14–24.

Westerweel, J., 1994. Efficient detection of spurious vectors in particle image velocimetry data. Exp. Fluids 16, 236–247.

Westerweel, J., Scarano, F., 2005. Universal outlier detection for PIV data. Exp. Fluids 39, 1096–1100.

Willert, C.E., Gharib, M., 1991. Digital particle image velocimetry. Exp. Fluids 10, 181–193.